Journal of Wind Engineering & Industrial Aerodynamics 240 (2023) 105501

Contents lists available at ScienceDirect

Journal of Wind Engineering & Industrial Aerodynamics

journal homepage: www.elsevier.com/locate/jweia

Aerodynamic characteristics of a high-rise building in a steady thunderstorm outflow-like flow field

Yang Li [a], Matthew S. Mason [b], Hao-Yu Bin [c], Yuan-Lung Lo [a,*]

[a] Department of Civil Engineering, National Taipei University of Technology, Taipei, Taiwan
[b] School of Civil Engineering, The University of Queensland, St. Lucia, Queensland, Australia
[c] Department of Civil, Chemical, and Environmental Engineering, DICCA Polytechnic School, University of Genova, Genoa, Italy

ARTICLE INFO

Keywords:
Thunderstorm
Downburst
Nose-like velocity profile
Multiple-fan wind tunnel
CAARC building

ABSTRACT

This paper investigates the aerodynamic characteristics of a high-rise building loaded by steady wind flows with different boundary layer profile shapes. The multiple-fan wind tunnel (MFWT) at Tamkang University was used to simulate a mean velocity field with a nose-shaped boundary layer profile, similar to that observed in thunderstorm outflows, and a standard boundary layer flow, both with 3–5% turbulence over the depth of the profile. A regular 'open terrain' boundary layer flow was also generated using spires and roughness blocks to enable comparison. Aerodynamic characteristics of the Commonwealth Aeronautical Advisory Research Council (CAARC) building loaded by each of these flow fields through a range of incidence angles were measured, analyzed, and compared. Results showed that pressures on the windward face of the building largely reflected the dynamic pressure in the incident wind field. Pressures on faces within the separated wake region were less easily explained. Incident mean velocity and turbulence profiles, as well as building orientation, were all found to influence measured wind loads and forcing spectra on these faces. Of particular interest was a significant reduction in cross-wind forcing observed in the simulated outflow-like winds, largely believed to occur because the lower elevation of strong winds in this profile limits the development of a separation vortex up the height of the building. It was also found that the estimated building response was almost universally lower in the outflow-like flow field when compared with the boundary layer cases.

1. Introduction

Wind-induced damage to structures is caused by various meteorological phenomena. Among these conditions, thunderstorms are the dominant phenomenon in many parts of the world. The modern discussion on thunderstorm structure can be traced back to the 1950s when Byers and Braham (1949) showed that the evolution of mesoscale thunderstorms consists of three stages and occur on a scale of a few kilometers. In the 1980s, Fujita (1985) discovered and described the formation of thunderstorm downbursts and the resulting shallow layer of strong winds they produce when downdrafts impinge on the surface of the earth and diverge in starburst-like patterns. Based on accumulated monitored data from three projects: NIMROD (1978), JAWS (1982), and MIST (1986), Fujita (1990) described the nose-shaped (or wall jet) velocity profile of the divergent radial outflows from downbursts and discussed their salient features. More recent observational studies have extended our understanding of these outflow boundary layers and, in particular, have highlighted the variability that can exist in these profiles from event to event and also within a given outflow itself (Canepa et al., 2020; Gunter and Schroeder, 2015; Lambardo et al., 2014).

In wind engineering, the non-stationary and non-Gaussian load effects of thunderstorm winds have been popular topics when considering engineering design for safety and economic efficiency. A framework proposed by Kwon and Kareem (2009) categorized the overall dynamic effects of structures due to a thunderstorm wind into four elements: (1) kinematic effects, (2) rise-time effects, (3) non-stationary turbulence effects, and (4) transient aerodynamic effects. Much recent literature has focused on (2) and (3). For example, Chen and Letchford (2004a) evaluated the response of a single-degree-of-freedom system due to a non-stationary wind by decomposing the thunderstorm wind into a time-varying mean component and a zero-mean fluctuating component. Chen and Letchford (2004b) then gave a maximum dynamic magnification factor to determine the ratio between the dynamic and static responses. Choi and Hidayat (2002), Chay and Albermani (2005), and

* Corresponding author.
E-mail address: yllo@mail.ntut.edu.tw (Y.-L. Lo).

https://doi.org/10.1016/j.jweia.2023.105501
Received 14 December 2022; Received in revised form 27 June 2023; Accepted 3 July 2023
Available online 11 July 2023

Holmes et al. (2005) conducted similar works. Solari et al. (2015) improved the treatment of the fluctuating component by considering the product of the slowly-varying standard deviation and a rapidly-varying stationary Gaussian zero-mean process and unit standard deviation. Other researchers have investigated advanced analytical techniques on this topic, for instance, the evolutionary spectral density, wavelet transform, and time-domain simulations (Huang and Chen, 2009; Huang et al., 2013), and the processes are now relatively well understood and modeled.

For element (4), the transient aerodynamic effects, early works, such as Sarpkaya and Kline (1982), Sarpkaya and Ihrig (1986), and Shirato et al. (2009), have discussed the aerodynamic coefficient variations of two-dimensional bluff bodies under accelerating or impulsively started flows. Results showed that the transient effects on the drag or lift coefficients depend on the breadth/depth ratio, or the depth/width ratio, of the immersed bluff bodies and the wind attack angles. More recently, Takeuchi and Maeda (2013) conducted wind tunnel experiments to investigate the drag and lift coefficients on a three-dimensional elliptic cylinder under accelerating flow. The same authors then went on to study the loading of several building models under similar conditions (Takeuchi et al., 2016). Like earlier studies, this work found that substantially larger loads than in steady flow conditions could occur over parts of a building provided acceleration rates were high enough. However, Yang and Mason (2019), through a study exploring the transient load effects on three two-dimensional rectangular prisms under a range of accelerating flows, suggest that the levels of flow acceleration experienced during thunderstorm outflows are unlikely to be high enough to generate significant 'overshoots' of steady flow loading for most structures. Irrespective, more research is required to adequately understand the true nature of transient aerodynamic effects as they relate to thunderstorm loading of buildings.

For element (1) of the Kwon and Kareem (2009) framework (kinematic effects), numerous studies have been undertaken to explore how the mean load effects on buildings change in different flow fields. Early research by Baines (1963), for example, showed that wind pressures and flow patterns around a tall building model changed substantially depending on whether it was placed in a uniform or a simulated atmospheric boundary layer flow field. Studies specifically relating to thunderstorm-generated winds have also been undertaken, with many of these using experimental impinging jets to study loads on low-rise buildings (Jubayer et al., 2019), cubes (Letchford and Chay, 2002; Mason et al., 2009) and numerous other structures with differing roof geometries (Jesson et al. 2015a, 2015b). In addition, Butler et al. (2010) used an actively controlled multi-fan wind tunnel to study pressures on prismatic building models in an atmospheric boundary layer as well as a thunderstorm outflow-like wind field with a nose-like mean velocity profile. Despite these studies all concluding that outflow-like wind fields generate loading that differs from regular atmospheric boundary layer wind loads, much is still to be learned about *why* these differences exist.

Given the above, the primary aim of this paper is to investigate how wind loading on a generic tall building changes when immersed in a regular atmospheric boundary layer and a simulated thunderstorm outflow-like wind field. We will then speculate why these differences may exist and hopefully provide some useful insight for future work to build upon. For this study, three different wind fields are generated in the Tamkang University multi-fan wind tunnel, and the resulting wind loads on a model of the Commonwealth Aeronautical Advisory Research Council (CAARC) building (Wardlaw and Moss, 1970) are measured and studied. The three profiles simulated include a standard "open terrain" atmospheric boundary layer profile, a nose-shaped velocity profile like that expected during thunderstorm outflows, and a second atmospheric boundary layer profile with low levels of turbulence throughout its depth (similar to levels in the nose-shaped profile). Wind pressures, forces, and moments applied to the model building for each of the flow cases and through a range of incidence angles are analyzed and discussed. Spectral densities and estimates of dynamic structural response using random vibration theory are also used to explore the differing nature of load and response that exist for each of the cases.

The remainder of this paper is set out as follows. Section 2 describes the experimental setup in the multiple-fan wind tunnel and presents the characteristics of the simulated flow fields and building model. Section 3 details the research findings and discusses the aerodynamic characteristics of wind pressures/force coefficients on the building model for all incident velocity fields and angles of attack. Section 3 also details the estimated wind-induced response of the full-scale CAARC building due to the simulated wind fields. The observed relationships between the incident velocity field and both the loading coefficients and response are discussed throughout section 3. Finally, Section 4 concludes the paper and provides a summary of key findings.

2. Experimental setup

2.1. Flow simulation

Experiments were conducted in the multiple-fan wind tunnel (MFWT) at the Wind Engineering Research Center, Tamkang University. The MFWT is an actively controlled blow-down tunnel with seventy-two individual motor-fan units, twelve in column and six in row. Each motor-fan unit comprises a servo motor and a 0.22 m diameter fan within its own independent channel. The tunnel has a 2:1 vertical contraction section downwind of the 72 fans that can generate a maximum wind speed of 16 m/s and a turbulence intensity of around 3% at the inlet of the test section. The test section has dimensions of 1.32 m in width and height and is 5.6 m in length downwind of the inlet. Fig. 1 shows a schematic diagram of the MFWT with the model location for the current tests indicated. The test section is equipped with a turntable that allows for building model rotation. All internal tunnel surfaces are timber or glass and are notionally smooth.

The target flows in this study are 1) a standard "open terrain" boundary layer flow (hereafter: BLC), based on terrain C specified in the Taiwanese wind code (MoIT, 2015), 2) a boundary layer flow with the same mean velocity profile as BLC but with low turbulence intensity in the approaching winds (hereafter: ABL), and 3) a nose-shaped mean velocity profile, representative of a thunderstorm outflow-like wind field, exhibiting low levels of turbulence throughout its depth (hereafter: TS). The BLC flow case is designed to provide a reference set of results representative of loading in a typical atmospheric boundary layer. The other two flows, i.e., ABL and TS, are designed to explore the profile-shape effects on the wind forces and associated responses of a high-rise building.

To generate each of these flow conditions, the rotational frequency of the 72 fans was individually adjusted until the desired mean velocity profile was produced. Fan frequencies were held constant for each test; however, some lateral variability in fan frequency was introduced to promote mixing within the flow. Fig. 2 shows the rotation frequency set for each of the 72 fans for the three target flow conditions. The numbers shown in each box indicate the rotation frequency for each fan. The frequency distributions generally reflect the target mean wind speed profiles, with low fan frequencies at elevations where low mean velocities are required and high fan frequencies at elevations where higher velocity is needed. A relatively uniform distribution of fan frequencies was applied for the BLC case, with surface-mounted roughness blocks and triangular spires used to shape the boundary layer. Fig. 3 shows the arrangement of these features in the tunnel for the BLC flow case.

Fig. 4 shows the mean wind speed profiles for each of the simulated flows. The BLC and ABL mean U velocity profiles agree well with the accepted open terrain characteristics of a power law with an index of 0.15 (terrain C in Taiwanese wind code). The TS flow was designed to replicate the empirical outflow velocity profile proposed by Wood et al. (2001) and given in Equation (1). In this equation, δ is the height where $0.5U_{max}$ occurs and $erf()$ is the error function. Fig. 4 shows a good replication of this profile, with the maximum velocity occurring at an

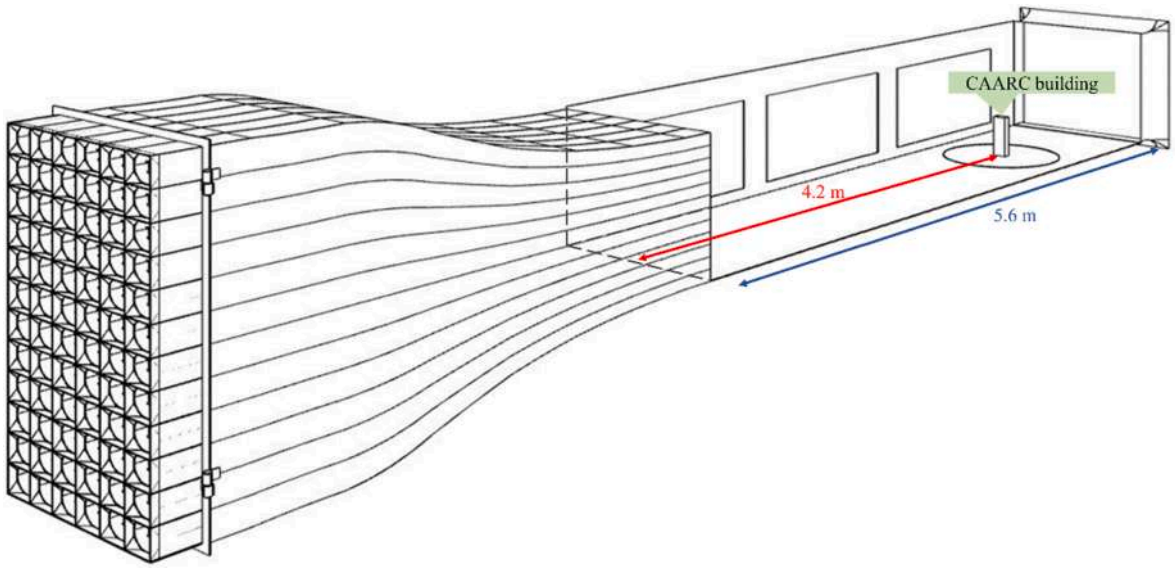

Fig. 1. Schematic diagram of the multiple-fan wind tunnel at Tamkang University.

4273	4244	4113	4332	4012	4195
3558	4023	4043	3813	3883	3747
3468	3699	3940	3931	3761	3783
3465	3683	3828	3801	3878	3803
3501	3579	3764	3762	3795	3991
3820	3688	3829	3904	4008	4213
4147	3973	3967	4108	4302	4834
3977	3842	3709	3953	4249	4640
4627	4084	3993	4203	4426	4627
4405	3963	3854	3948	4415	4405
4173	3558	3798	3909	4054	4681
3811	3545	4020	3844	3899	4142

(a) BLC

4739	4289	3649	3604	4610	4942
4001	3885	3705	3781	4066	4227
3963	3823	4048	3981	4002	4322
3927	3779	3940	3926	3853	4330
3713	3654	4260	4124	3912	4203
3685	3569	4171	4184	3841	4379
3532	3509	4031	4077	3759	4282
3481	3448	3809	3826	3771	4176
3241	3368	3707	3662	3671	3915
3229	3210	3509	3398	3500	3672
2918	2906	3150	3060	3141	3303
2303	2659	2810	2733	2407	2334

(b) ABL

461	345	455	552	430	545
523	358	649	759	489	520
680	607	804	862	654	743
899	779	1034	1069	891	908
994	942	1118	1276	1081	1106
1267	1192	1534	1561	1318	1519
1518	1475	1847	1818	1617	1833
1865	1844	2210	2154	2056	2323
2255	2328	2635	2561	2573	2730
2887	2876	3180	3070	3141	3290
3656	3624	3838	3750	3905	4126
3612	4179	3974	3905	3917	3697

(c) TS

Fig. 2. Rotation frequency (revolutions per minute) of each fan in the MFWT array for the (a) BLC, (b) ABL and (c) TS target flows.

elevation of approximately 100–150 mm. When using the geometric scale discussed in Section 2.2, this elevation equates to 40–60 m in full-scale, which is of an order similar to those observations for numerous events in the field (Hjelmfelt, 1988; Lambardo et al., 2014; Canepa et al., 2020). In addition, the TS flow case was designed to have the same maximum mean wind speed, $U_{max} = 10.5$ m/s, as the ABL and BLC flow cases and further, so that the depth-averaged velocity below 457 mm (height of the test model) was the same for each test case. Approximately zero mean wind speeds in the lateral (V) and vertical directions (W) was observed in each of the simulated flows.

$$U(z) / U_{max} = 1.55\left(\frac{z}{\delta}\right)^{1/6}\left[1 - erf\left(0.7\frac{z}{\delta}\right)\right] \quad (1)$$

Fig. 5 shows the turbulence intensity profiles for the three simulated flows. The BLC flow simulated in the MFWT shows Iu values ranging from just below 20% at the tunnel floor to approximately 7% at an elevation of 457 mm (height of building model). The Iu profile proposed by AIJ (2015) is also shown, with a reasonable agreement between it and the simulated BLC profile shapes. However, a relatively uniform underestimation of approximately Iu = 0.05 is shown for the BLC case, which in large part is due to the under-production of large-scale gusts in the MFWT, as discussed later in this section. This difference was deemed acceptable for this work, given that the primary focus is on comparisons between the ABL and TS cases. The ABL and TS flows display lower turbulence intensities over the profile depth than in the BLC flow case. Values of approximately 7–8% near the surface that vary between this value and 3% over the profile height are shown. This relatively low level of turbulence was intentionally simulated (at least in the TS case) to conceptually replicate the low turbulence conditions observed during the Lubbock-Reese Rear Flank Downdraft and discussed by Holmes et al. (2008). In that case, observed Iu values near the surface were 9–11%, which, while marginally higher than those simulated here, are roughly replicated. For the TS flow, a localized maximum in each of the turbulence intensity profiles is observed at approximately 250 mm. This maximum coincides with the elevation of the maximum negative gradient in the mean velocity profile and thus indicates shear-induced

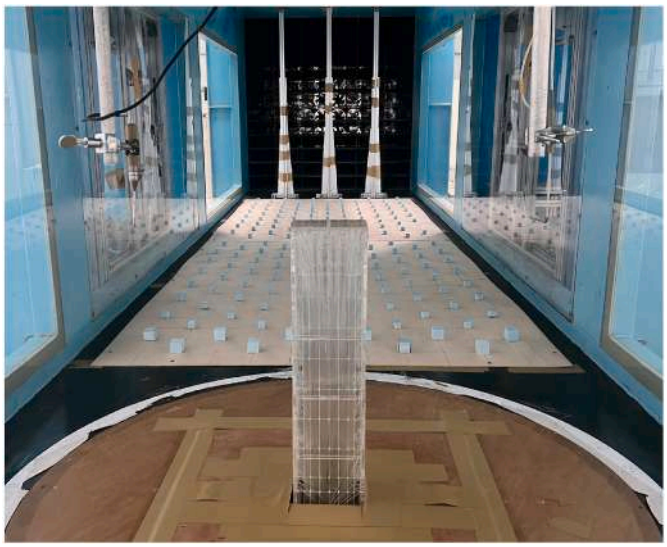

Fig. 3. Wind tunnel setup for the BLC flow case.

turbulence and is reasonably expected. Similar turbulence intensity profiles and magnitudes are shown for both the TS and ABL profiles. Again, this matching was intentionally done so that subsequent wind loading comparisons could focus on the influence of mean velocity profile-shape effects and as much as possible rule out any influence that turbulence may have on those loads.

The fluctuating wind speeds at elevations of z = 150 mm and z = 450 mm are plotted in the format of wind speed spectra in Fig. 6. These heights coincide with the maximum mean wind speeds in the TS and ABL flows, respectively. The theoretical von Karman Spectra is also shown for comparison. As expected, the ABL and TS flows both show relatively low turbulence energies over the low frequency range before decreasing as n > 20 Hz. Given their low turbulence intensity values, it is also unsurprising that they sit well below the von Karman spectra of a generic atmospheric boundary layer. When comparing BLC results generated in the MFWT with the von Karman spectra, good replication is evident for the high frequency range above n ≈ 10 Hz, but the spectral energy is lower in the low-frequency range. This underrepresentation exists because the size of each of the 72 fan channels limits the maximum scale of turbulence that can be generated within the tunnel. Even with the triangular spires implemented to aid the generation of larger eddies, the turbulence in the approaching winds was unable to be built up to a scale that could match the low frequency range of the von Karman spectrum. Nevertheless, the inertial sub-range of the spectrum shows a nearly −5/3 slope, implying that the BLC setting in the MFWT is still suitable for studying resonant response estimation of structures.

2.2. Building model information

The building model adopted in this study was the Commonwealth Aeronautical Advisory Research Council (CAARC) building (Wardlaw and Moss, 1970) with a 1/400 length scale, as shown in Fig. 7. A total of 384 pressure taps were distributed at 11 elevations up the model and on the rooftop surface. The SCANIVALE micro-pressure scanning system simultaneously measured pressures over the model at a sampling rate of 300 Hz for a period of 1200 s. Using length and velocity scales determined for the test, this corresponded to 120 runs of 10-min field samples, with this number collected to ensure statistical stability. Wind incidence was tested between 0 and 90° for the subsequent discussions of aerodynamic characteristics. Fig. 8 shows two views of the building model coordinate system, including the building model, the relative position of the building model and the 72 fans, and the angle of attack.

2.3. Data processing

Usually, measured pressures from a wind tunnel model are normalized using the mean velocity pressure at the model height or free stream height to obtain aerodynamic coefficients. In boundary layer flows, the mean wind speed at the model height is the maximum value since it follows the power or logarithmic law. Applying this mean wind speed to discuss dimensionless aerodynamic characteristics, such as the pressure or force coefficient, is convenient. However, the maximum mean wind speed for the TS profile is near the ground (in this case, 1/3 the building height), with velocities at model eaves height approximately 60% of this maximum (Fig. 4). This means that if the traditional coefficient definition is applied, excessively large pressure and force coefficients will result and examining the profile-shape effects would be difficult.

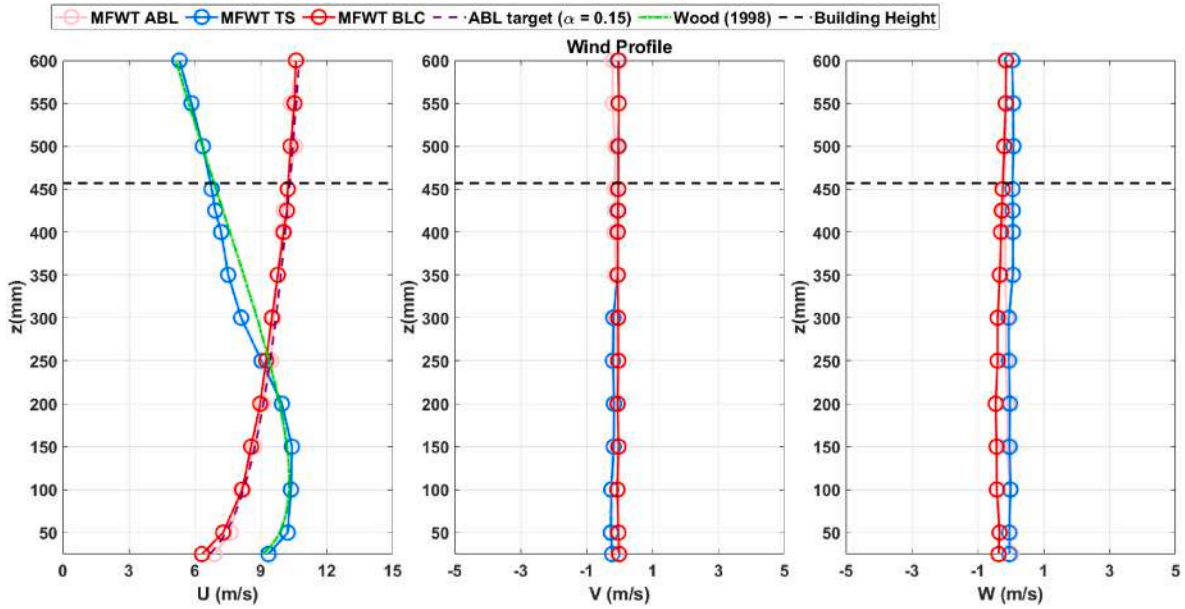

Fig. 4. Vertical profiles of mean along wind, U, across-wind, V and vertical, W, wind velocities for BLC, ABL and TS flow cases.

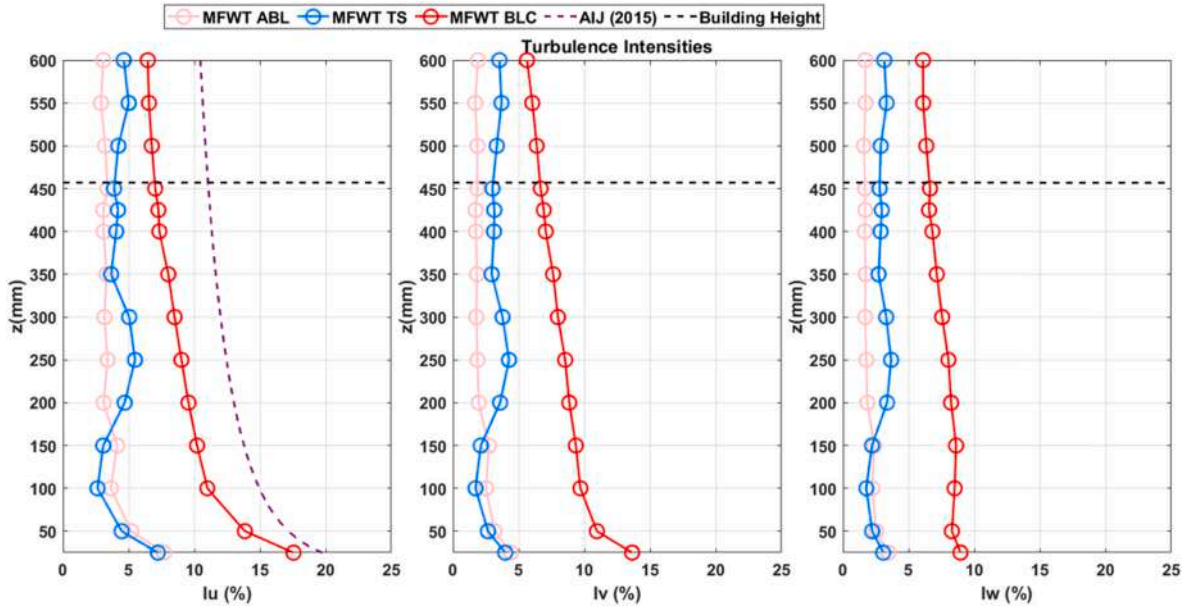

Fig. 5. Vertical profiles of mean longitudinal, Iu, crosswind, Iv and vertical, Iw, turbulence intensities for BLC, ABL and TS flow cases.

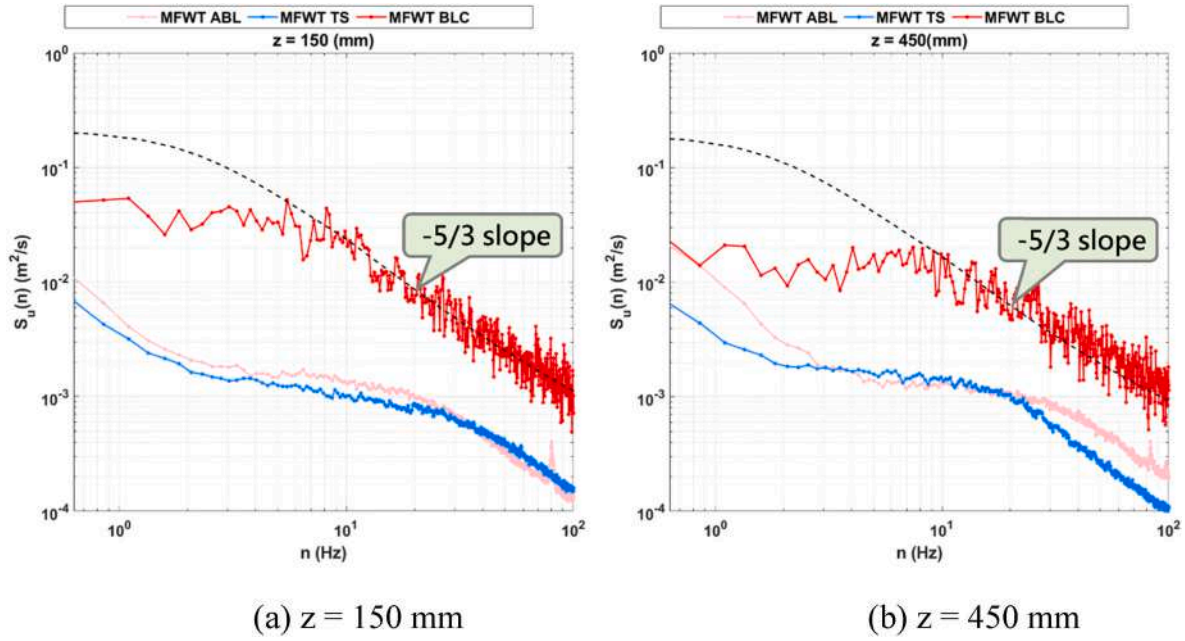

Fig. 6. Measured velocity spectra at (a) z = 150 mm and (b) z = 450 mm for the BLC, ABL and TS cases, with the von Karman Spectrum also shown.

Therefore, measured pressures are normalized by the corresponding maximum mean wind speeds, U_{max}, within each specific test case profile, using:

$$C_{p,i}(t) = \frac{p_{i,total}(t) - \overline{p}_{static}}{1/2\rho U_{max}^2} \tag{2}$$

where $p_{i,total}(t)$ is the measured instantaneous total pressure at the i-th tap on the model, $\overline{p}_{static}$ is the mean reference static pressure, ρ is the air density (assumed to be 1.2 kg/m^3), and U_{max} is the maximum mean wind speed for each test case. That is, the mean wind speed at the building height is adopted for the BLC and ABL flows, while for the TS flow, the mean wind speed at 1/3 building height is used. Given $U_{max} = 10.5$ m/s for all cases, resulting pressure coefficients are readily comparable across all test cases. The reference static pressures for the ABL and TS flows are measured by Cobra probes shown in Fig. 8(a) where correspond to the maximum mean wind speeds.

Force and moment coefficients are then calculated by integrating pressure coefficients over the model. Equations (3)–(5) are used to do this for forces in the building-relative x direction, $C_{fx}(Z,t)$, at a given elevation Z, building-relative y direction, $C_{fy}(Z,t)$, and moments around the z axis, $C_{mz}(Z,t)$, respectively.

$$C_{fx}(Z,t) = \sum_{i=1}^{m} \left(C_{p,i,Face\ A}(Z,t) - C_{p,i,Face\ C}(Z,t)\right) \bullet \left(\frac{\Delta w_i}{w_{AC}}\right) \tag{3}$$

$$C_{fy}(Z,t) = \sum_{i=1}^{n} \left(C_{p,i,Face\ B}(Z,t) - C_{p,i,Face\ D}(Z,t)\right) \bullet \left(\frac{\Delta w_i}{w_{BD}}\right) \tag{4}$$

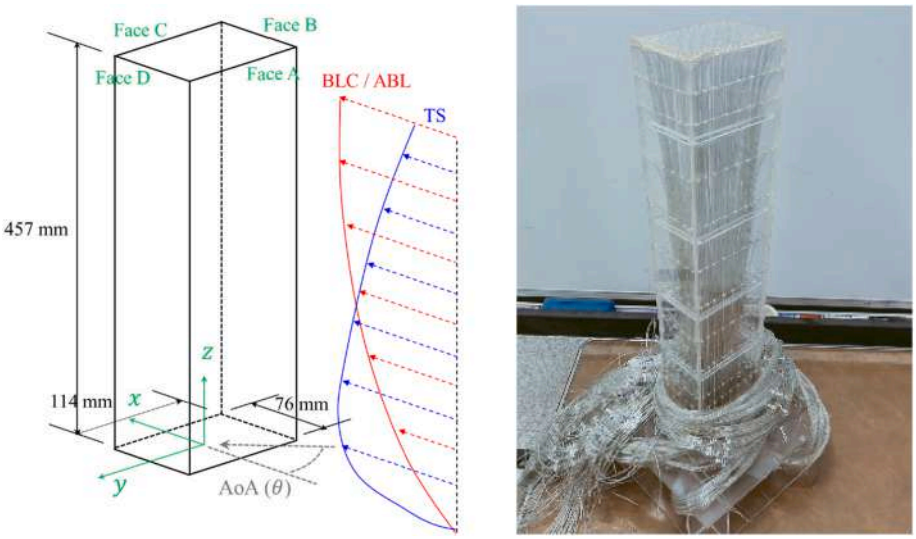

Fig. 7. Diagram of the CAARC building model and its photo.

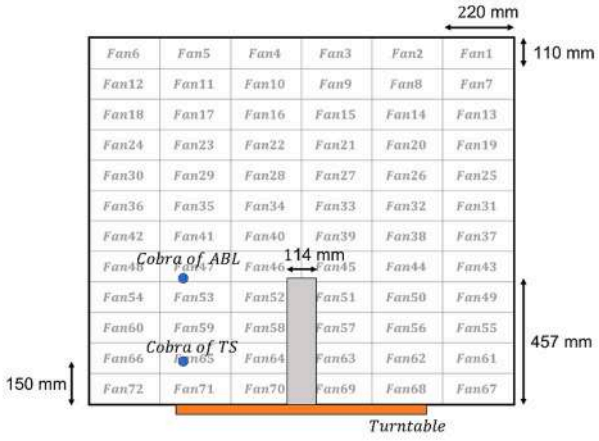

(a) Relative position of the model, the 72 fans and reference probe locations for ABL and TS tests (back view).

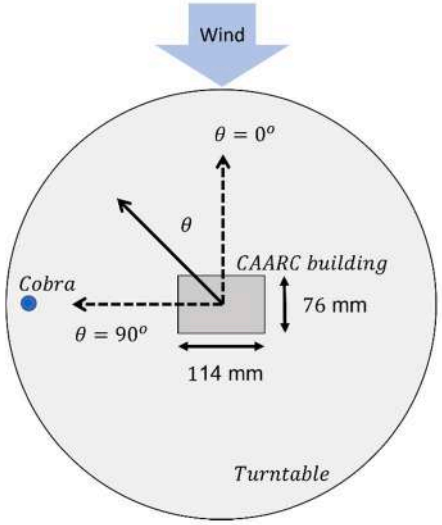

(b) Angle of attack (top view).

Fig. 8. The coordinate system of the building model.

$$C_{mz}(Z,t)=\sum_{i=1}^{m}\left(\begin{array}{l}C_{p,i,Face\ A}(Z,t)\bullet\left(\frac{\Delta w_i}{w_{AC}}\right)\bullet\left(\frac{\Delta l_i}{w^*}\right)+\\ C_{p,i,Face\ C}(Z,t)\bullet\left(\frac{\Delta w_i}{w_{AC}}\right)\bullet\left(\frac{\Delta l_i}{w^*}\right)\end{array}\right)+\sum_{i=1}^{n}\left(\begin{array}{l}C_{p,i,Face\ B}(Z,t)\bullet\left(\frac{\Delta w_i}{w_{BD}}\right)\bullet\left(\frac{\Delta l_i}{w^*}\right)+\\ C_{p,i,Face\ D}(Z,t)\bullet\left(\frac{\Delta w_i}{w_{BD}}\right)\bullet\left(\frac{\Delta l_i}{w^*}\right)\end{array}\right) \quad (5)$$

In these equations, x is the direction perpendicular to Face A and C, y is the direction perpendicular to Face B and D, and z is the vertical axis (Fig. 7). Nine pressure taps were installed on Face A at each elevation, while on the opposite face, Face C, another nine taps were installed at corresponding positions. Therefore, to calculate the instantaneous wind force coefficient in the x direction at elevation Z, $C_{fx}(Z,t)$, instantaneous pressure coefficient differences, $C_{p,i,Face\ A}(Z,t)-C_{p,i,Face\ C}(Z,t)$, at nine tap positions ($i=1\sim m$, $m=9$) were weighted by their representative widths $\Delta w_i/w_{AC}$, and then summed over the model width. The above estimation process is repeated for the 11 tap ring elevations on the building model to show the wind forces in the x direction. Equation (4) follows the same concept for estimating the wind force coefficients in the y direction. Equation (5) describes the torsion coefficients around the z axis by summing up all the contributions from pressure taps at the same elevation. Δl_i represents the force arm from the tap to the geometric center of the cross-section. w^* is the geometric mean of widths of Face A and B. Equations (6)–(8) are finally used to convert forces at each elevation to the overturning moment coefficients in the x and y directions and about the z axis.

$$C_{B,my}(t)=\sum_{ring=1}^{11}C_{fx}(Z,t)\bullet\left(\frac{Z}{H}\right) \quad (6)$$

$$C_{B,mx}(t)=\sum_{ring=1}^{11}C_{fy}(Z,t)\bullet\left(\frac{Z}{H}\right) \quad (7)$$

$$C_{B,mz}(t)=\sum_{ring=1}^{11}C_{mz}(Z,t) \quad (8)$$

2.4. Response estimation

In this study, wind-induced responses of a full-scale version of the CAARC building due to each of the different flows are estimated. All building information is given in Table 1 for converting the experimental aerodynamic features from lab scale to field scale. The CAARC building model is converted to a field-scale building at a length scale of 1/400 and the mass density of the building is assumed to be 300 kg/m^3. Since the first vibration mode of a high-rise building usually dominates the dynamics of the building, it is convenient to consider that only the first mode in the three directions contributes to the wind-induced responses.

Table 1
Building information for conversion from lab-scale experiments.

Geometry	Width B (m)	Depth D (m)	Height H (m)
Model (WT)	0.114	0.076	0.457
Building (Field)	45.6	30.4	182.8
Similarity factor (Length scale)	λ_L 1/400		
Sampling condition		Lab scale	
	Rate n_S	300 Hz	
	Increment Δt	0.0033 s	
	Recording T	1,200 s	
Mass density $\rho=300$ kg/m^3	$m_{x,floor}$ (kg)	$m_{y,floor}$ (kg)	$m_{\varphi,floor}$ (kg·m^2)
	1.13×10^6	1.13×10^6	3.35×10^8
Tuned fundamental frequency*	$n_{x,field}$ (Hz)	$n_{y,field}$ (Hz)	$n_{\varphi,field}$ (Hz)
	0.286	0.315	0.429

To simplify things here, we also assume the first mode is linear. The x-direction (the direction passing through Face A to Face C) fundamental frequency of the first mode for the CAARC building is assumed to follow the empirical formula of 50/H proposed by Tamura (2012). The x-direction fundamental frequency is 0.286 Hz. The y-direction (the direction passing through Face B to Face D) fundamental frequency is taken to be 0.315 Hz based on a convenient assumption of the depth/width ratio, while the fundamental torsional frequency, φ, around the z-axis is assumed to be 1.5 times the frequency in the x direction, i.e., $\varphi=0.429$ Hz. In practice, the fundamental frequencies in the x-direction and y-direction are usually designed close to each other. Further, the fundamental frequency in the torsional direction is usually assumed to be 1.3–1.5 times the lower frequency of the two translational directions. The damping ratio is set to be 1% for all three directions. The lumped mass is 1.13×10^6 kg in the two translational directions, and the rotational inertial mass is 3.35×10^8 kg m^2 in the torsional direction for each building floor.

To generally discuss the profile-shape effects on the responses, the reduced velocity is assumed to vary from 4 to 8 in the following discussions, which corresponds to different design wind speed levels for the CAARC building. Table 2 lists the reduced velocities and corresponding information for response estimations. Equation (9) defines the reduced velocities in this study.

$$U_r=\frac{U_{max}}{n^*\bullet\sqrt{BD}} \quad (9)$$

where U_{max} is again the maximum mean wind speed for a flow case; n^* is the lower fundamental frequency of two translational directions (in this case, $n^*=n_x$); $\sqrt{BD}$ is the characteristic width of the building.

The spectral analysis method of a generalized single-degree-of-freedom system is applied to estimating the wind-induced responses. Equation (10) defines the governing equation of motion for a high-rise building under the assumption of a continuously mass-distributed linear system.

$$m(z)\ddot{u}(z,t)+c\dot{u}(z,t)+k(z)u(z,t)=f(z,t) \quad (10)$$

where m, c, k are the systematic mass, damping, and stiffness; $u(z,t)$ is the lateral displacement against height z at time instant t, and $f(z,t)$ is the external wind loading. Based on the orthogonality of vibration modes estimated from the eigenvalue analysis, Equation (10) can be further transformed to Equation (11), the generalized governing equation of the *jth* mode:

$$\widetilde{M}_j\ddot{\widetilde{U}}_j(t)+\widetilde{C}_j\dot{\widetilde{U}}_j(t)+\widetilde{K}_j\widetilde{U}_j(t)=\widetilde{F}_j(t) \quad (11a)$$

where

$$\widetilde{M}_j=\varphi_j^T m\varphi_j \quad \widetilde{C}_j=\varphi_j^T c\varphi_j \quad \widetilde{K}_j=\varphi_j^T k\varphi_j \quad \widetilde{F}_j(t)=\varphi_j^T f(t) \quad (11b)$$

In Equation (11), φ_j is the *jth* vibration mode and $\widetilde{U}_j(t)$ is the *jth*

Table 2
Assumed reduced velocities and corresponding information.

Maximum mean wind speed (Lab scale) $U_{max,lab}$ (m/s)	10.5				
Characteristics width $\sqrt{BD}$ (m)	37.2				
Fundamental frequency $n_{x,field}$ (Hz)	0.286*				
Reduced velocity U_r	8	7	6	5	4
Maximum mean wind speed (Field scale) $U_{max,field}$ (m/s)	85.1	74.5	63.8	53.2	42.6
Velocity scale factor λ_U	0.123	0.141	0.165	0.197	0.246
Time scale factor λ_T ($\times10^{-2}$)	2.033	1.773	1.515	1.269	1.016
Converted frequency $n_{x,lab}$ (Hz)	14.07	16.13	18.88	22.54	28.15
Converted frequency $n_{y,lab}$ (Hz)	15.49	17.77	20.79	24.82	31.00
Converted frequency $n_{\varphi,lab}$ (Hz)	21.10	24.20	28.32	33.81	42.22

generalized coordinate. Generally, for a high-rise building, the first model dominates its oscillation behavior when excited by earthquakes or winds. The first mode shape can be assumed to be $\varphi_1 = z/H$ for simplicity. The generalized force $\widetilde{F}_j(t)$ in Equation (11) is then written in the format of the overturning moment in Equation (12). In this study, $M(t)$ is the measured overturning moment, which for an angle of attack of 0° uses $M_y(t)$ for the estimation of the along-wind response x, $M_x(t)$ for the estimation of the across-wind response y, and $M_\varphi(t)$ for the estimation of the torsional response φ. H is the building height.

$$\widetilde{F}_1(t) = \frac{z}{H} f(z,t) = \frac{M(t)}{H} \tag{12}$$

As a result, the governing equation of the motion for a high-rise building can be calculated using Equation (13) in conjunction with Equation (11).

$$\ddot{\widetilde{U}}(t) + 2\xi_1\omega_1\dot{\widetilde{U}}(t) + \omega_1^2\widetilde{U}(t) = \frac{M(t)}{\widetilde{M}_1 H} = \frac{q_H BH}{\widetilde{M}_1} C_M(t) \tag{13}$$

In Equation (13), ξ_1 is 1% damping ratio for x, y, φ responses. ω_1 is the circular frequency of the first mode and $\omega_1 = 2\pi n_0$. n_0 can be replaced with n_x, n_y, n_φ for x, y, φ responses. $\widetilde{M}_1$ is the generalized mass of the first mode and can be replaced with $\widetilde{M}_{1,x}$, $\widetilde{M}_{1,y}$, $\widetilde{M}_{1,\varphi}$ for x, y, φ responses. The reference velocity pressure $q_H = 1/2\rho U_H{}^2$ is $q_{max} = 1/2\rho U_{max}{}^2$, as defined in the denominator in Equation (2) in this study. $C_M(t)$ is the base moment coefficient and can be replaced with $C_{B,M_y}(t)$, $C_{B,M_x}(t)$, $C_{B,M_z}(t)$ for x, y, φ response estimations. The response variance obtained by integrating the response spectra can consist of two components – the background and resonant components, Equation (14). The background component can be derived from the approaching fluctuating wind based on the quasi-static assumption; the resonant component is estimated by the narrow-band assumption of a Gaussian distributed variable.

$$\begin{aligned}
\sigma_x^2 &= \left(\frac{q_{max}BH^2}{(2\pi n_x)^2\widetilde{M}_{1,x}H}\right)^2 \left[\left(C'_{B,M_y}\right)^2 + \left(\frac{\pi n_x}{4\xi_1}\right) S_{C'_{B,M_y}}(n_x)\right] \sigma_y^2 \\
&= \left(\frac{q_{max}BH^2}{(2\pi n_y)^2\widetilde{M}_{1,y}H}\right)^2 \left[\left(C'_{B,M_x}\right)^2 + \left(\frac{\pi n_y}{4\xi_1}\right) S_{C'_{B,M_x}}(n_y)\right] \sigma_\varphi^2 \\
&= \left(\frac{q_{max}BDH^2}{(2\pi n_\varphi)^2\widetilde{M}_{1,\varphi}H}\right)^2 \left[\left(C'_{B,M_z}\right)^2 + \left(\frac{\pi n_\varphi}{4\xi_1}\right) S_{C'_{B,M_z}}(n_\varphi)\right]
\end{aligned} \tag{14}$$

Together with Equation (14), the peak responses can be estimated by Equation (15) with the properly assumed peak factors.

$$\hat{x} = \bar{x} \pm g_x\sigma_x \;\; \hat{y} = \bar{y} \pm g_y\sigma_y \;\; \hat{\varphi} = \bar{\varphi} \pm g_\varphi\sigma_\varphi \tag{15}$$

The sign ± in Equation (15) represents the possible maximum or minimum depending on the mean value. Results for wind incidence from 0° to 90° are reported. The mean responses in the three building-relative directions are estimated by dividing the generalized mean forces by corresponding generalized stiffnesses, as defined in Equation (16).

$$\bar{x} = \bar{F}_{1,x}/K_{1,x} \;\; \bar{y} = \bar{F}_{1,y}/K_{1,y} \;\; \bar{\varphi} = \bar{F}_{1,\varphi}/K_{1,\varphi} \tag{16}$$

where $\bar{F}_{1,x}$, $\bar{F}_{1,y}$, and $\bar{F}_{1,\varphi}$ are the mean components of the generalized forces in the x, y, and φ directions (Equation (12)). $K_{1,x}$, $K_{1,y}$, and $K_{1,x\varphi}$ are the generalized stiffnesses. In this study, the mean responses in the x and y directions are translational displacements while the mean response in the φ direction is rotational angles.

To integrate all the observed profile-shape effects caused by the nose-like flow, Equation (17) defines the construction of the x-direction peak response, an alternative expression from the conjunction of Equations (14) and (15). The symbol x in Equation (17) can be replaced with y or φ for the other two responses. The peak factor for the background component, g_B, is assumed to be 2.5 for a 10-min field sample (Tamura and Kareem, 2013). The peak factor for the resonant component, g_R, is calculated by Equation (18), where T equals 600 (seconds) and n_0 is fundamental frequencies n_x, n_y, n_φ in the x, y, φ directions.

$$\hat{x} = \bar{x} \pm \sqrt{g_B{}^2\sigma_{x,B}{}^2 + g_R{}^2\sigma_{x,R}{}^2} \tag{17a}$$

where

$$\sigma_{x,B}{}^2 = \left(\frac{q_{max}BH^2}{(2\pi n_x)^2\widetilde{M}_{1,x}H}\right)^2 \left[\left(C'_{M_y}\right)^2\right] \tag{17b}$$

$$\sigma_{x,R}{}^2 = \left(\frac{q_{max}BH^2}{(2\pi n_x)^2\widetilde{M}_{1,x}H}\right)^2 \left[\left(\frac{\pi n_x}{4\xi_1}\right) S_{C_{M_y}}(n_x)\right] \tag{17c}$$

and

$$g_R = \sqrt{2\ln(n_o T)} + \frac{0.577}{\sqrt{2\ln(n_o T)}} \tag{18}$$

3. Results and discussions

3.1. Aerodynamic force characteristics

3.1.1. Mean pressure coefficients

The ensemble averages of 120 mean pressure coefficients from the 120 10-min equivalent records are plotted into contours in Fig. 9 for the (a) BLC, (b) ABL, and (c) TS flows at the angle of attack = 0°, i.e., the depth/width ratio = 0.67. Note that contours are only shown for the area of each face that had pressure taps, so do not extend to the extremities of each. The mean pressure coefficients over the windward faces generally follow the profile shapes of approaching winds for each case. That is, for the BLC and ABL cases, pressure coefficients are largest near the top of the face (~0.85H, similar to that shown in Baines (1963)) as this is where velocities are highest, while for TS, the peak pressure is at an elevation of approximately $H/3$, which mimics the peak in the TS velocity profile. When inspecting the BLC and ABL results in more detail though, despite no apparent discrepancies in the mean wind speed profiles (Fig. 4), it is found that high positive pressure coefficients extend further down the face in the ABL flow than in the BLC flow. The higher turbulence intensities in the approaching winds of the BLC flow thus appear to affect the mean pressure coefficient gradient on this face. We speculate that the higher turbulence encourages flow to be more readily diverted down the face (or down and around) rather than directly around the building, thus leading to a smaller stagnation region in the BLC flow.

Inspecting the side (B and D) and leeward (C) faces, which for an angle of attack of 0° lie within the separated wake, similar coefficient distributions are shown for the BLC and ABL cases. However, pressure coefficients on both the side and leeward face are approximately 10–20% lower (i.e., higher suction pressures) for the ABL case. This is thought to occur because the increased turbulence in the BLC case allows for greater entrainment of fluid into the wake region, which consequently increases the pressures in this region (Hearst et al., 2016). For both cases, suction pressures show a maximum near the base of the side wall and at the trailing edge of the upper region of the side and leeward faces. A minimum in suction pressures is also observed near the center of the leeward wall, as evident in many previous studies of the CAARC building (e.g., Tanaka and Lawen, 1986). Pressure coefficients on the wake faces for the TS case are, however, considerably different. A decreasing pressure gradient is observed from the leading edge at the base of the side wall to the trailing edge at the top of the wall. An increase in pressure with elevation on the leeward face is also evident. The presence of the maximum pressures on the side and leeward faces at similar elevations, located just below the elevation of the maximum windward face pressures, does suggest similar flow mechanisms may exist. Here it is hypothesized that these maxima are, as in the earlier cases, linked to flow being directed downward below the stagnation

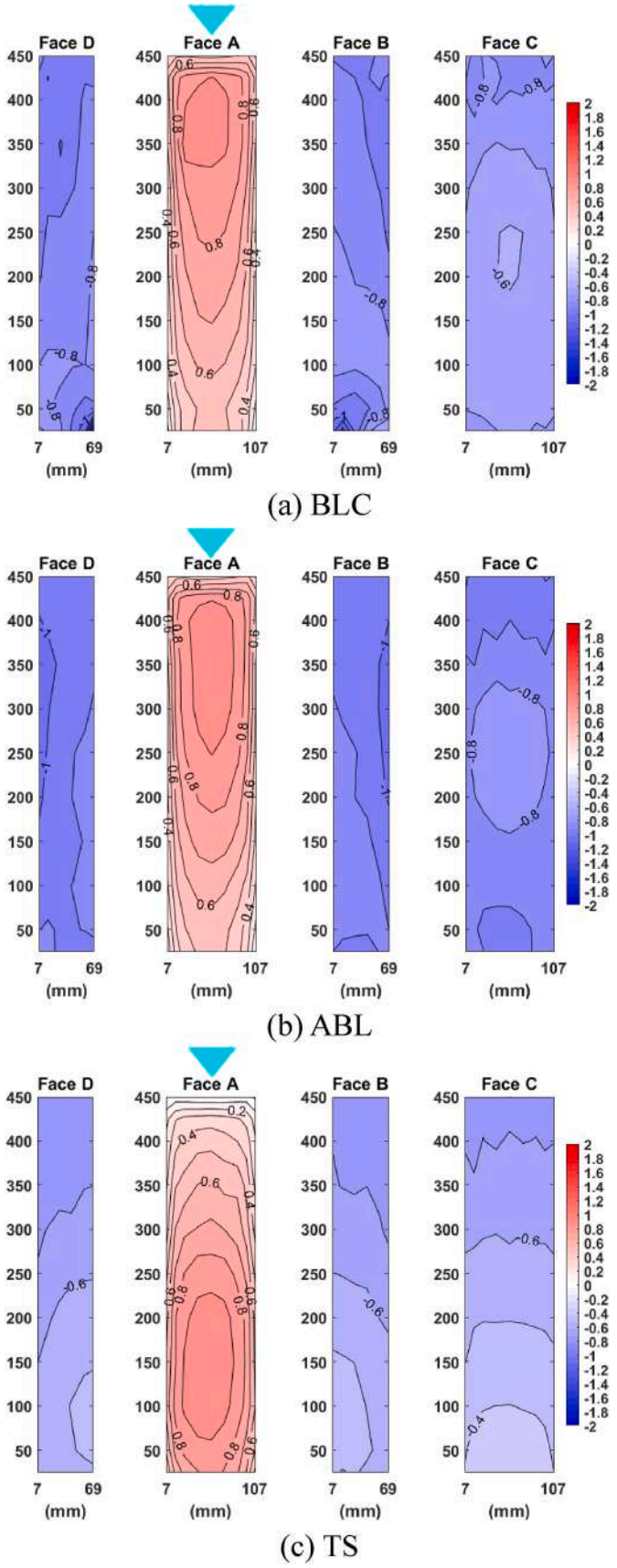

Fig. 9. Contours of mean pressure coefficients for BLC, ABL, and TS flows with the angle of attack = 0° Blue triangle indicates the windward face.

region and around the side of the model. Despite this similarity, though, a notably different wake appears to develop for the TS case when compared with both BLC and ABL flow cases. The mean pressure coefficients over the side face in the TS flow are more like that in the BLC flow. An evident decreasing tendency is observable when the elevation decreases. The BLC and ABL flows share a radial pattern in their mean pressure coefficients over the leeward face. The latter indicates larger negative pressure coefficients. Unlike the BLC and ABL flows, a stepwise gradient distribution is shown in the TS flow. As the elevation increases, the negative pressure coefficient magnitude increases, followed by the gradient lines over the side faces. When the angle of attack turns 90°, i.e., the depth/width ratio = 1.5, patterns in mean pressure distributions in Fig. 10 remain similar to 0°, particularly on the windward face, but some differences in the distribution magnitude over the wake faces is observed.

3.1.2. *Fluctuating pressure coefficients*

Fluctuating (Root-mean-square) pressure coefficients over the surfaces of the building model with an angle of attack = 0° are presented in Fig. 11. The windward face of the BLC flow shows a relatively uniform distribution of R.M.S pressure coefficients, but with values 2–3 times higher than for than the ABL or TS flow. This difference in values reflects the distribution of turbulence intensities shown in Fig. 6, with the increased turbulence in the BLC flow leading to higher buffeting effects on the body. Over the side faces, the three flows show symmetric but different distribution patterns of R.M.S values. In the BLC flow, high R.M.S pressure coefficients are found near the middle area of the building side faces, and it is seen that the nearer to the rear edge of the side face, the higher the fluctuations are (at least at higher elevations). In the ABL flow, the R.M.S coefficients decrease up the height of the model, forming clear horizontal gradient lines. This observation again supports the assertion made when viewing the mean pressure coefficients that despite similar flow structures being developed around the model in the ABL and BLC cases, the increase turbulence in the BLC flow does lead to some modification of the flow field. Compared with the ABL and BLC flows, the TS results show relatively small magnitude R.M.S values over the side faces with values similar to the fluctuations on the windward face observed. This suggests a more stable flow regime is setup for this flow case and may point to a reduced presence and influence of cross-wind loading processes, such as vortex shedding. This will be explored further in later sections of this paper. Further discrepancy between flow cases is seen in the R.M.S pressure coefficient distributions in the leeward faces. The highest values for both the BLC and ABL cases are seen on the sides of the face with a minimum in the center of the face over the height of the model. This pattern, along with that observed in the mean pressure coefficient distribution, suggests the presence of vertical vortices in the wake and is expected for this type of structure. However, no such distribution is observed for the TS case and the weak observed wake fluctuation will inevitably result in weaker fluctuating along-wind force and reduce the contribution from the background winds.

In Fig. 12, the R.M.S pressure coefficients of the building model with the angle of attack = 90° are presented to examine the depth/width ratio effects in the ABL and TS flows. Influenced by the turbulence intensities in the approaching winds, the R.M.S pressure coefficient distributions over four faces in the BLC flow are similar to those with the angle of attack = 0° in Fig. 11. However, for the ABL flow, the R.M.S pressure coefficient distributions over the side faces (A and C) are more like those in the BLC flow, albeit at about 50–60% of the magnitude, rather than retaining the same features as observed in the ABL flow with the angle of attack = 0°. Meanwhile, the distributions over the windward and leeward faces for the BLC and ABL flow conditions remain relatively consistent whether the angle of attack is 0° or 90°. The TS flow has the same R.M.S pressure coefficient distribution over the windward face whether the angle of attack = 0° or 90°. On the side faces, a horizontal gradient of the R.M.S coefficients remains, with increasing values

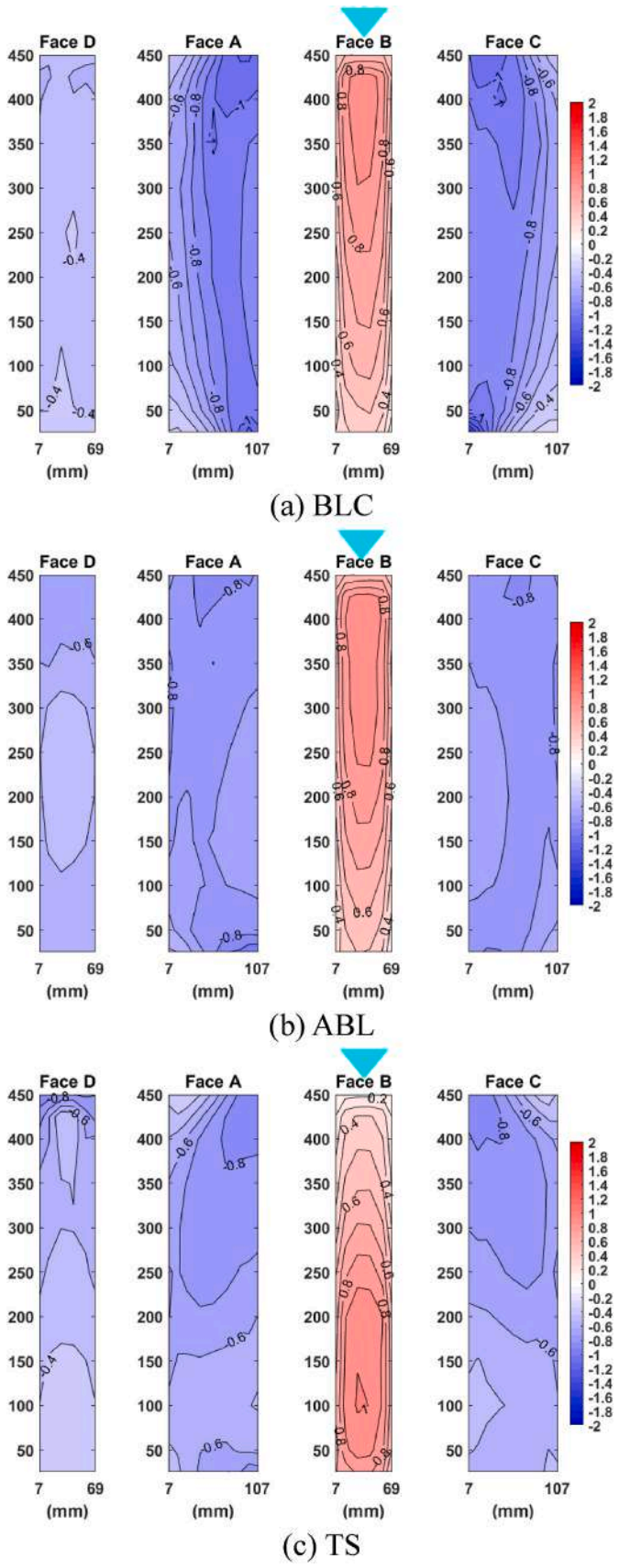

Fig. 10. Contours of mean pressure coefficients for BLC, ABL, and TS flows with the angle of attack = 90° Blue triangle indicates the windward face.

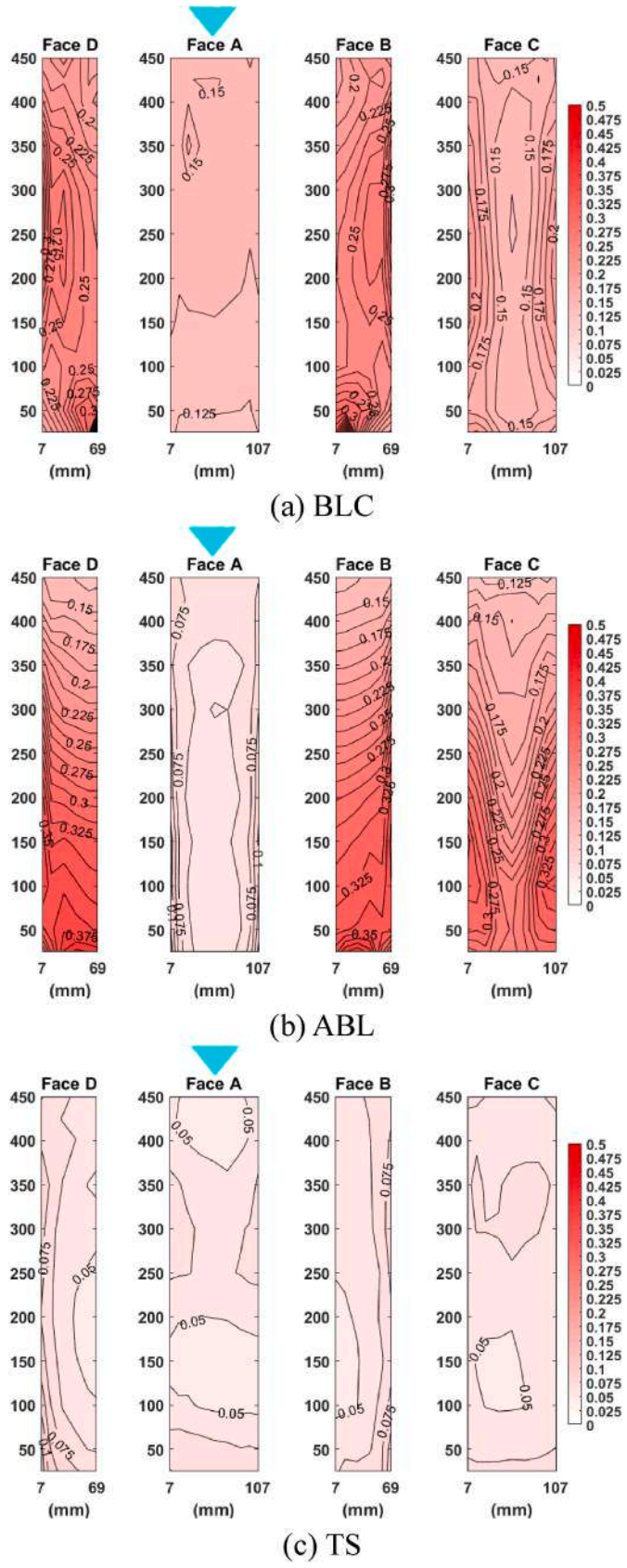

Fig. 11. Contours of R.M.S pressure coefficients for (a) BLC, (b) ABL, and (c) TS flows with the angle of attack = 0°. Blue triangle indicates the windward face.

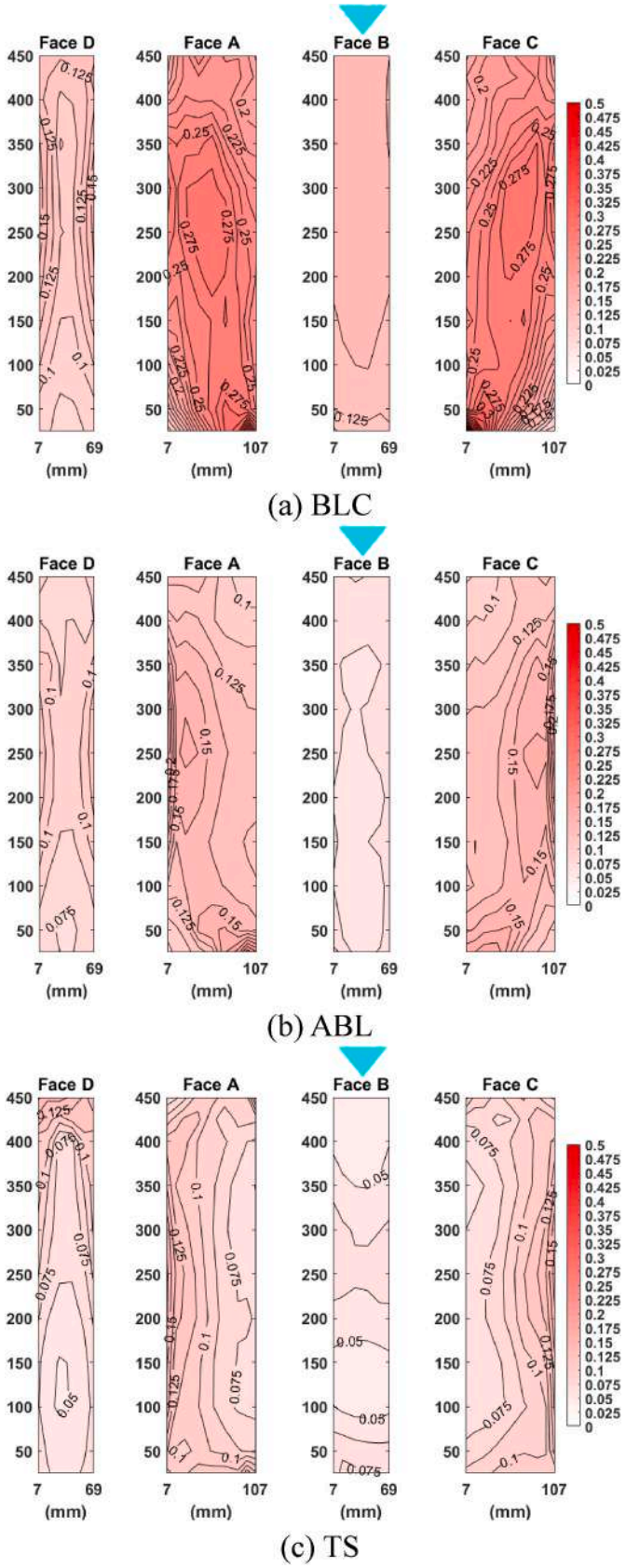

Fig. 12. Contours of R.M.S pressure coefficients for (a) BLC, (b) ABL, and (c) TS flows with the angle of attack = 90°. Blue triangle indicates the windward face.

towards the rear edge. The more uniform distribution up the leading edge of these faces when compared with 0° suggests greater organization of flow in this region for this angle of incidence. The distribution over the leeward face shows small fluctuations at elevations near that of U_{max} and large fluctuations near the top of the model. Even though the leeward face has a relatively narrower area, the distribution of the R.M.S coefficients form a noticeably different pattern to the BLC and ABL flows and a somewhat different distribution to that seen for an angle of attack = 0°. Such observations indicate that differences in loading, and therefore by inference the flow structures that induce it, is dependent not only on the flow case but also the angle of attack = 0° and 90°, i.e., the depth/width ratio effects.

3.1.3. Mean force coefficients

Fig. 13 shows the mean wind force coefficients calculated for each level of taps on the model building using Equations (3) and (4) for the angles of attack = 0° and 90° and the three flow cases. In the along-wind direction, the ABL flow with the angle of attack = 0° has larger mean wind force coefficients ($\overline{C}_{fx}$ in Fig. 13(a)) over the building height range than the BLC and the TS flows, which corresponds well with the larger negative pressures indicated in the leeward face in the ABL flow in Fig. 10. When the angle of attack turns to 90° ($\overline{C}_{fy}$ in Fig. 13(b)), the discrepancy between the ABL and the BLC flow results is reduced, but the same profile shape is maintained and the almost uniform offset between the two is maintained. For the low turbulence cases, ABL and TS, unlike for the angle of 0° where $\overline{C}_{fx}$ is consistently higher for the ABL flow case, mean force coefficients over the lower half of the model in the 90° TS flow exceed that in the ABL flow. This again shows that the building depth/width ratio as well as the velocity profile shape can result in different along-wind forces distributions on the model. As expected for symmetrically loaded structures, forces in the across-wind and torsional directions ($\overline{C}_{fy}$, $\overline{C}_{mz}$ in Fig. 13(a) and $\overline{C}_{fx}$, $\overline{C}_{mz}$ in Fig. 13 (b)) show relatively consistent and nearly zero values for both angles of attack, irrespective of the depth/width ratio.

3.1.4. R.M.S force coefficients

Fig. 14 shows the root-mean-square (R.M.S) values of fluctuating wind force coefficients with the angle of attack = 0° and 90° for the three flows. In the along-wind direction, the BLC flow has higher RMS values over the building height than the other two flows, as expected. Comparing the ABL and TS flows with two different angles of attack indicates that the depth/width ratio of the building cross-section once again alters the significance of fluctuating forces. A higher R.M.S coefficient distribution is seen in the ABL flow with a smaller depth/width ratio (angle of attack = 0°), particularly near the base of the model. The TS flow results, while being of lower magnitude than ABL and BLC results, show values two to three times higher for the 90° case. This is particularly true over the lower part of the model where the fluctuating pressure coefficient values were noted to be small for the 0° orientation. The BLC flow has a more significant R.M.S value at the lower half of the building height range with the angle of attack = 0°; however, higher R.M.S values are more concentrated at the middle range of the building height. Like the BLC flow, the ABL flow has the same patterns with the angles of attack = 0° and 90°. The ABL flow has even higher R.M.S coefficients with the angle of attack = 0° than the BLC flow but less significant R.M.S coefficients when the angle of attack turns 90°. The R.M.S force coefficients in the torsional direction generally follow the tendencies seen in the across-wind direction given the same flow structures (e.g., vortex shedding) primarily drive these two loads.

3.1.5. Spectra of overturning moment coefficients

Figs. 15 and 17 show the spectra of overturning moment coefficients in the along-wind, across-wind, and torsional directions for the angles of attack = 0° and 90°. Here the spectra of overturning moment coefficients are obtained by calculating the power spectral densities of the

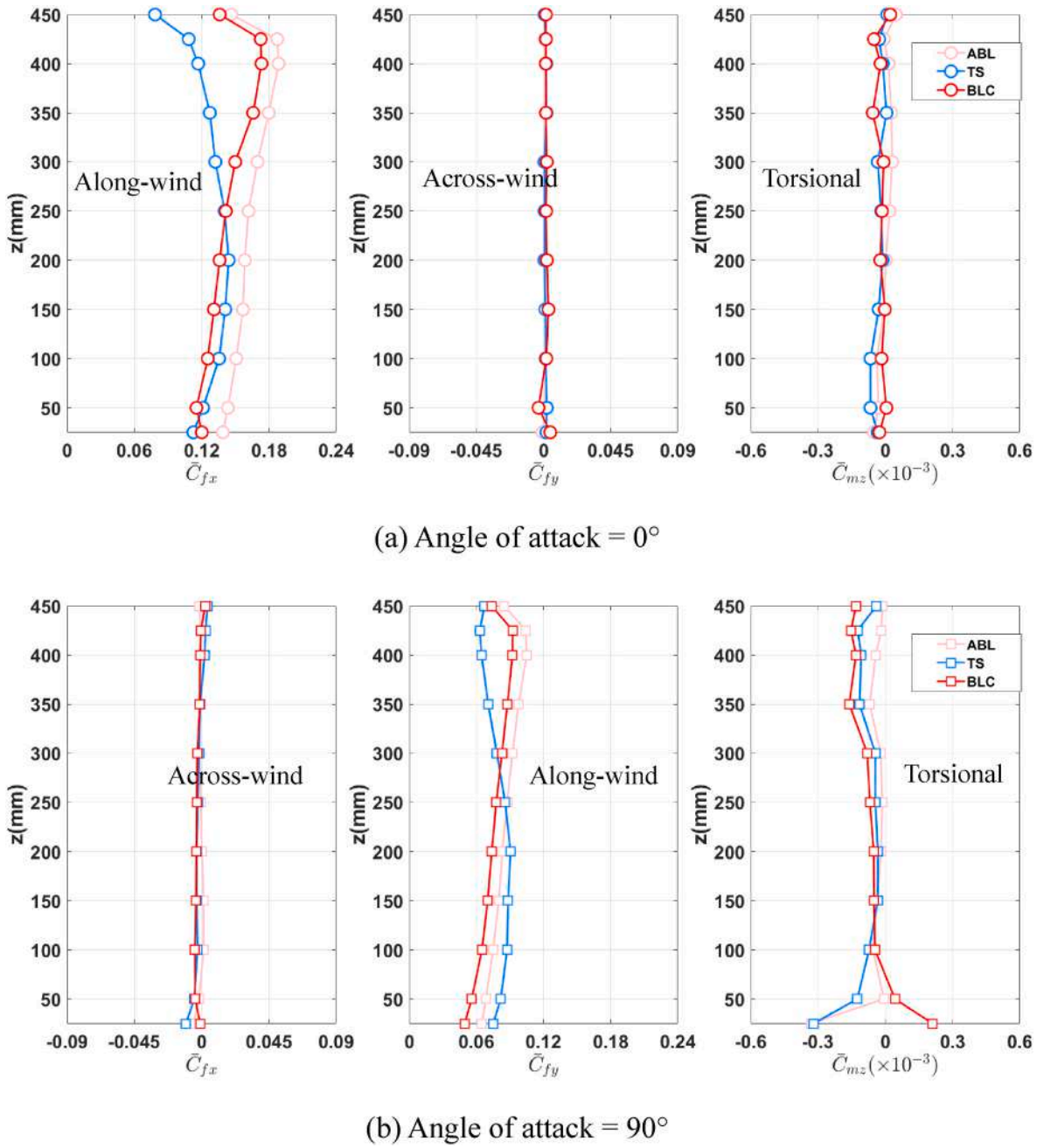

Fig. 13. Mean force coefficient distributions for BLC, ABL, and TS flows with an angle of attack of (a) 0° and (b) 90°.

overturning moment coefficients at the building base (Equations (6)–(8)).

The along-wind moment coefficient spectra are plotted in Fig. 15(a). Comparing the spectra for BLC and ABL cases, when the turbulence intensities in the approaching winds are low (i.e., ABL), the along-wind force coefficient spectrum shifts downward and shows a relatively sharp peak at 19.3 Hz. Given the relatively similar distribution of mean pressure for these two cases shown in Fig. 10, the presence of the along-wind peak in only one was unexpected. To investigate how this spectrum peak forms, the decomposed force coefficient spectra of Face A and Face C representing the windward force and the leeward spectra are shown in Fig. 16. From this figure it is evident that the peak is entirely driven by the building wake. It is also evident that the leeward face exhibits its peak at a frequency double that shown for the across-wind moment coefficient spectra in Fig. 15(b). This is a clear signature of the vortex shedding process, with some coupling of the along- and across-wind loading in this case. Although in the BLC flow the leeward face also exhibits a small peak, the dominant windward face obviously reduces the wake effect on the along-wind moment coefficient spectra. Continuing to inspect the across-wind spectra, the BLC case also shows a clear spike in the spectra but with a slight difference in shedding frequency than the lower turbulence ABL case. Interestingly, the along-wind and across-wind base moment coefficient spectra in the TS flow are both lower than in the other cases. There is no apparent peak near the same shedding frequency as the other two flows, which supports the earlier assertion that TS flow does not allow the same vortex structures to develop around the model as in the other cases. Practically, this seems to suggest that cross-wind forcing may be reduced in thunderstorm generated winds, assuming that a peak in the velocity profile exists below the height of a building. In Fig. 15(c), the same shedding frequencies of 9 Hz and 9.7 Hz are observed in the torsional moment spectra for the BLC and ABL flows as seen in Fig. 15(b) for the cross-wind

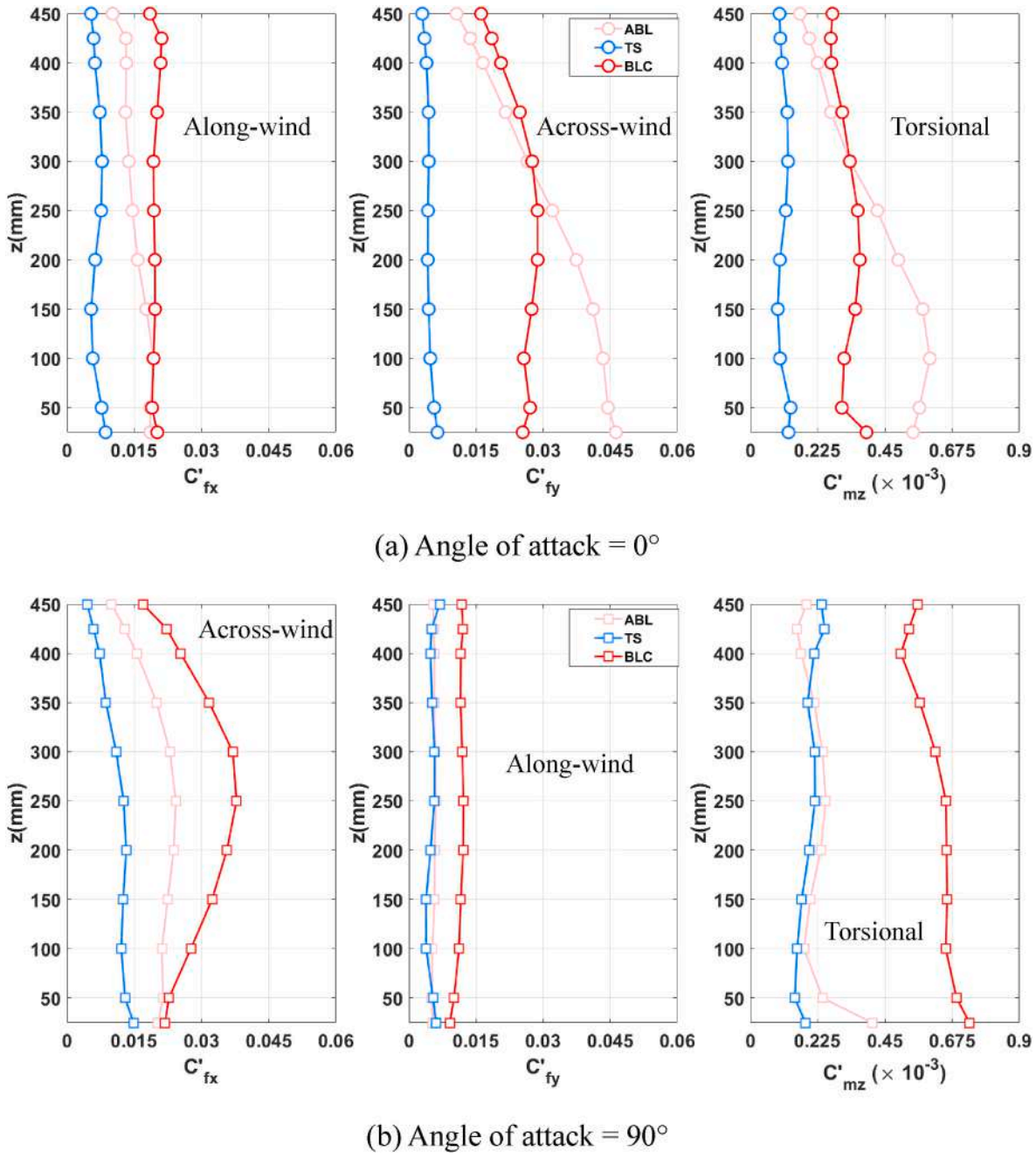

Fig. 14. R.M.S force coefficient distributions for BLC, ABL, and TS flows with an angle of attack of (a) 0° and (b) 90°.

moment. It is also of interest to note that a peak is evident at the triple frequency value of the shedding vortex at 28.8 Hz, which is possibly due to the coupling effects of the across- and torsional loading in the ABL flow. Coupling peaks observed in Fig. 15(a) and (c) explain how turbulence differences between the BLC and ABL flows affect the interaction behavior of vortex and wake formed around the building As for the TS flow, the spectrum shows a relatively significant drop from the other three flow cases. Although not dominant, two mild humps at the shedding frequency and the triple frequency can be observed.

Fig. 17 shows the base moment coefficient spectra of the model with the angle of attack = 90°. Fig. 17(a) shows that all three flows now exhibit peaks in the cross-wind direction at close but not identical frequencies (10.4–11.5 Hz). The differences observed between the ABL and BLC results are believed to be linked to the differing characteristics of the incident turbulence in these two flow cases (Nakamura and Ohya, 1984). In addition, compared to Fig. 15(b), the identified shedding frequencies for the BLC and ABL flows are 5–10% higher when the angle of attack = 90°. This increase is expected given the reduction in the cross-section width for this angle of attack (Choi and Kwon, 2003). Interestingly, the TS flow now produces a peak at approximately the same frequency as in the ABL flow. Comparing Figs. 15(b) and 17(a) shows that the TS flow exhibits different behavior when the angle of attack changes. To explore this, Fig. 18 shows the across-wind force spectra at several elevations for the two angles of attack. When the angle of attack equals 0°, force coefficient spectra at building elevations below 150 mm (approximately the elevation of the maximum in velocity profile, Fig. 4) show observable peaks while no clear peak can be found at higher building elevations. On the contrary, when the angle of attack equals 90°, all force coefficient spectra at various heights generally exhibit peaks, resulting in the dominant spectrum peak in Fig. 17(b). In

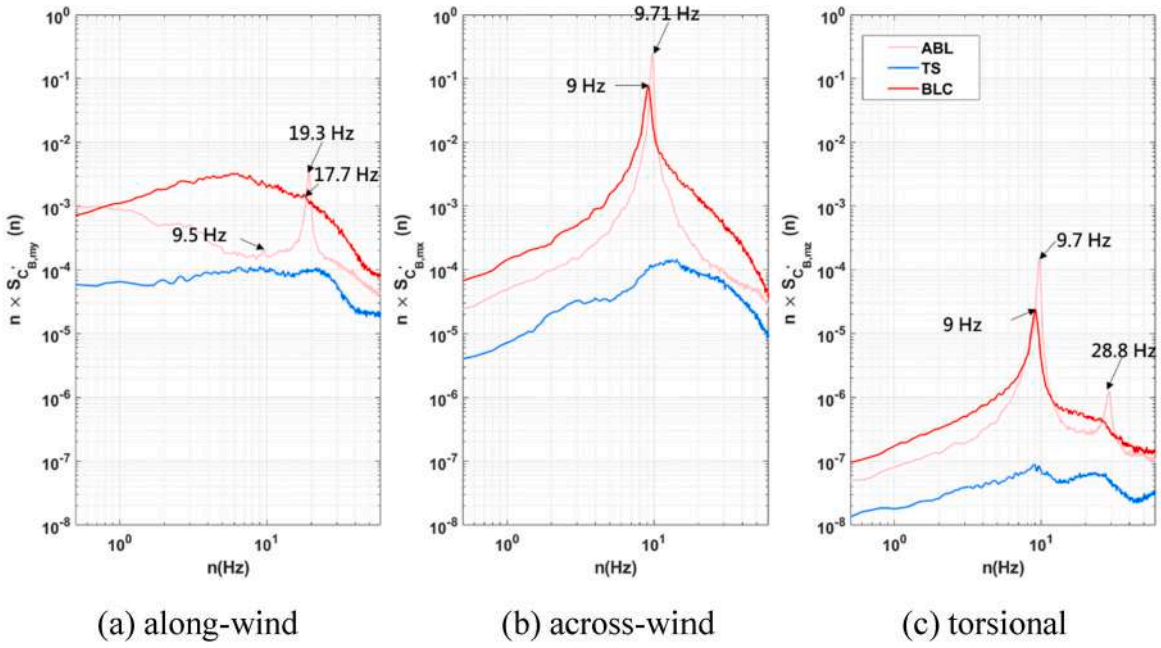

Fig. 15. Spectra of the (a) along-wind, (b) across-wind and (c) torsional base moments for BLC, ABL, and TS flows with the angle of attack = 0°.

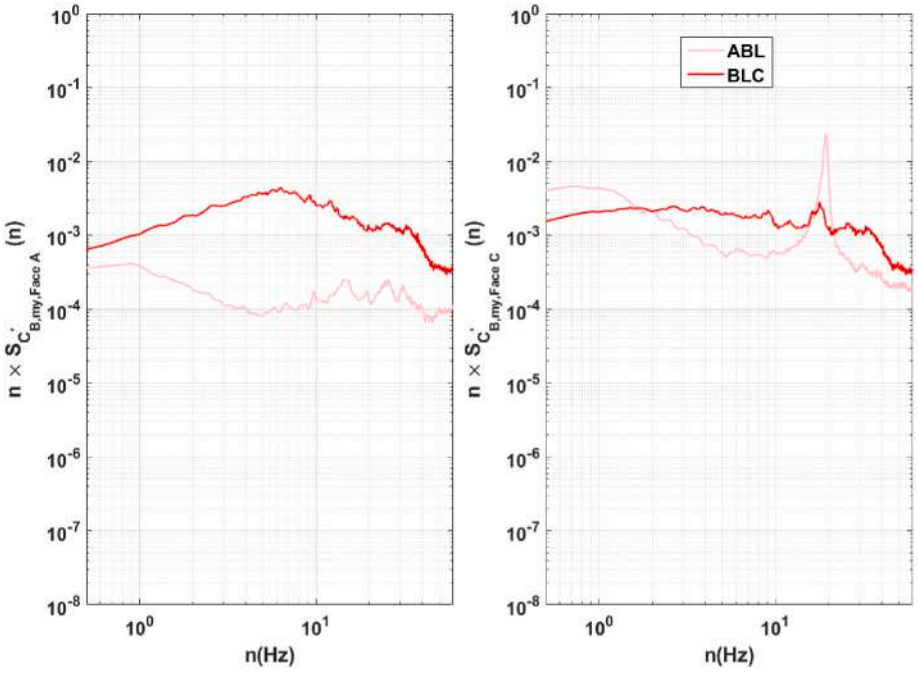

Fig. 16. Decomposed along-wind moment coefficient spectra for BLC and ABL flows with the angle of attack = 0° (Left: Face A; Right: Face C).

Fig. 17(b), the along-wind force coefficient spectra are plotted. With a larger depth/width ratio of the cross-section, the wake behind the building in the ABL flow does not show a double frequency peak due to the shedding vortex, leading to a generally smaller spectrum area for the across-wind force spectrum in the ABL flow. The torsional spectra in Fig. 17(c) differ from those in Fig. 15(c). A hump with a broader frequency range replaces the sharp spectrum peaks near the shedding frequencies for the two BLC flows. The spectrum peak at 11.3 Hz for the ABL flow remains, and a slight hump in the TS flow is still observed. On the other hand, all three flows have higher spectrum values in Fig. 17(c) within a broader and higher frequency range, the triple frequency area, than in Fig. 15(c).

3.2. Wind-induced responses

Previous sections have examined the aerodynamic characteristics due to the BLC, ABL, and TS flows. This section focuses primarily on the two low turbulence flow cases, ABL and TS, and explores how the response of the full-scale CAARC building would vary for these two types of wind field. Results for the BLC flow are, however, included in figures as a background reference. Results discussed include the mean responses, the background component responses, the resonant component responses under different reduced velocities, and the peak responses. Results for wind incidence from 0° to 90° are reported and discussed.

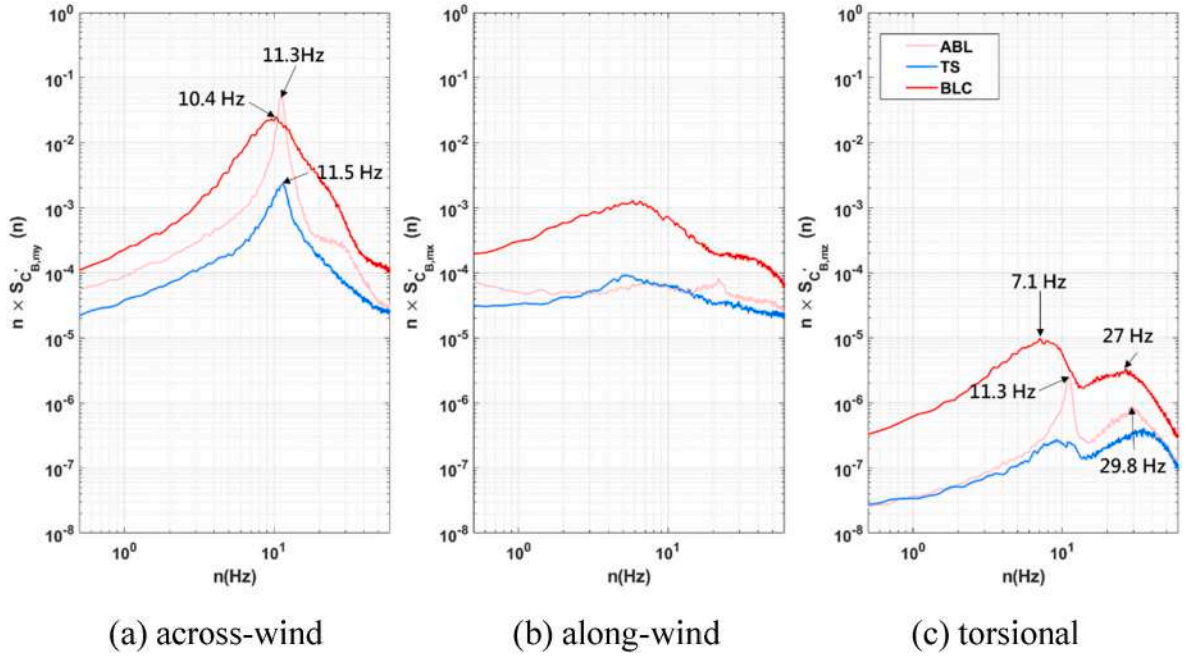

Fig. 17. Spectra of the (a) along-wind, (b) across-wind and (c) torsional base moments for BLC, ABL, and TS flows with the angle of attack = 90°.

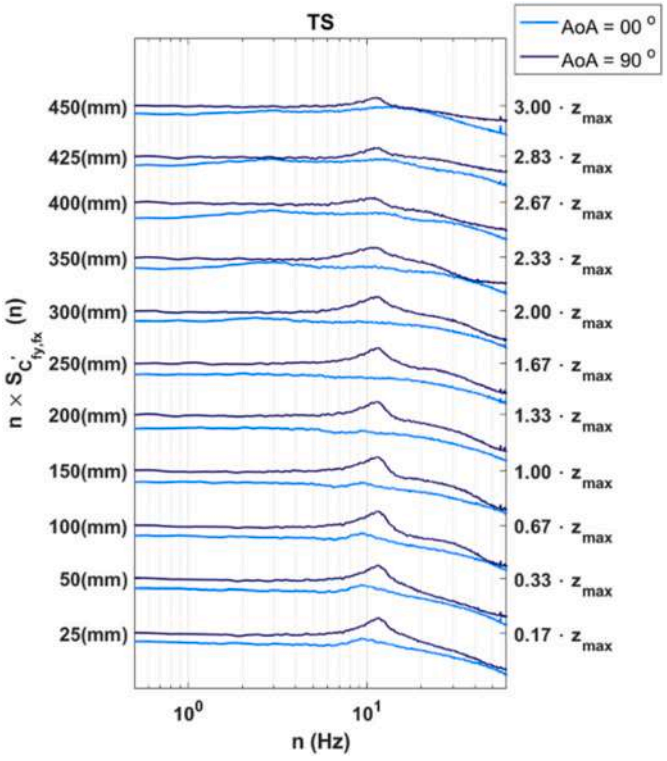

Fig. 18. Across-wind force coefficient spectra at different elevations for TS flow. ($z_{max} = 150\ mm$ is the height where U_{max} occurs).

3.2.1. Mean responses

Fig. 19 shows the mean responses in the simulated flows with respect to the variation of the angle of attack. The mean components of generalized responses are independent of reduced velocities, so only one curve is shown for each flow type. The mean responses in the ABL flow are generally larger than those in the TS flow when the dominant loading is in the along-wind direction. Among the *x*-direction responses, the exception to this observation is for mean responses with the angle of attack = 70° and 75° where the TS flow are slightly larger than in the ABL flow. Displacements are very low for these angles though so are of less concern from a loading standpoint. Similarly, the mean responses in the y-direction with the angle of attack = 10°–15° in the TS flow are slightly larger than those in the ABL flow. Torsional responses, φ in the TS flow exceed the ABL rotation only for the angle of attack of 85°. Other angles exhibit the same extent of results as the ABL flow. BLC results match TS responses across most angles and were generally less than in the lower turbulent ABL flow case.

3.2.2. Background component responses

Fig. 20 shows the square root of the first term in the bracket of Equation (14), $C'_{B,M}$, used to estimate the background component responses. Similar to the mean component responses, the background component responses are independent of the reduced velocities so only one curve is shown for each flow case. Among the *x* and *y* directions, the background component responses in the ABL flow are generally larger than, or at least equal to, those in the TS flow. For the torsional response, this generality remains except when the angle of attack is near 75°. Given that the TS and ABL flows simulated in this study have lower turbulence intensities in the approaching winds responses for both are lower than in the BLC flow, though this doesn't hold for all angles or all responses.

3.2.3. Resonant component responses

The resonant component responses in the TS and ABL flows are compared through the second term in the bracket of Equation (14), $(S_{C_{B,M}}(n_0))^{0.5}$. The dependence of this term on the fundamental frequencies of the building means different reduced velocities will generate different results so results for a series of reduced velocity are discussed. Fig. 21 shows the distributions of the squared spectrum values in the three directions with respect to the reduced velocity. In the *x* direction, the resonant component response in the TS flow is found to be larger than the ABL results with the angle of attack = 25°–45° when the reduced velocity is 8 and 40°, 70°, and 75° when the reduced velocity is 4. It is also interesting to point out that when the angle of attack = 0°–15°, under the condition of the lower turbulence intensities in the approaching winds, the reduced velocity of 5 produces a fundamental frequency closer to the shedding frequency shown in Fig. 15(a). As such,

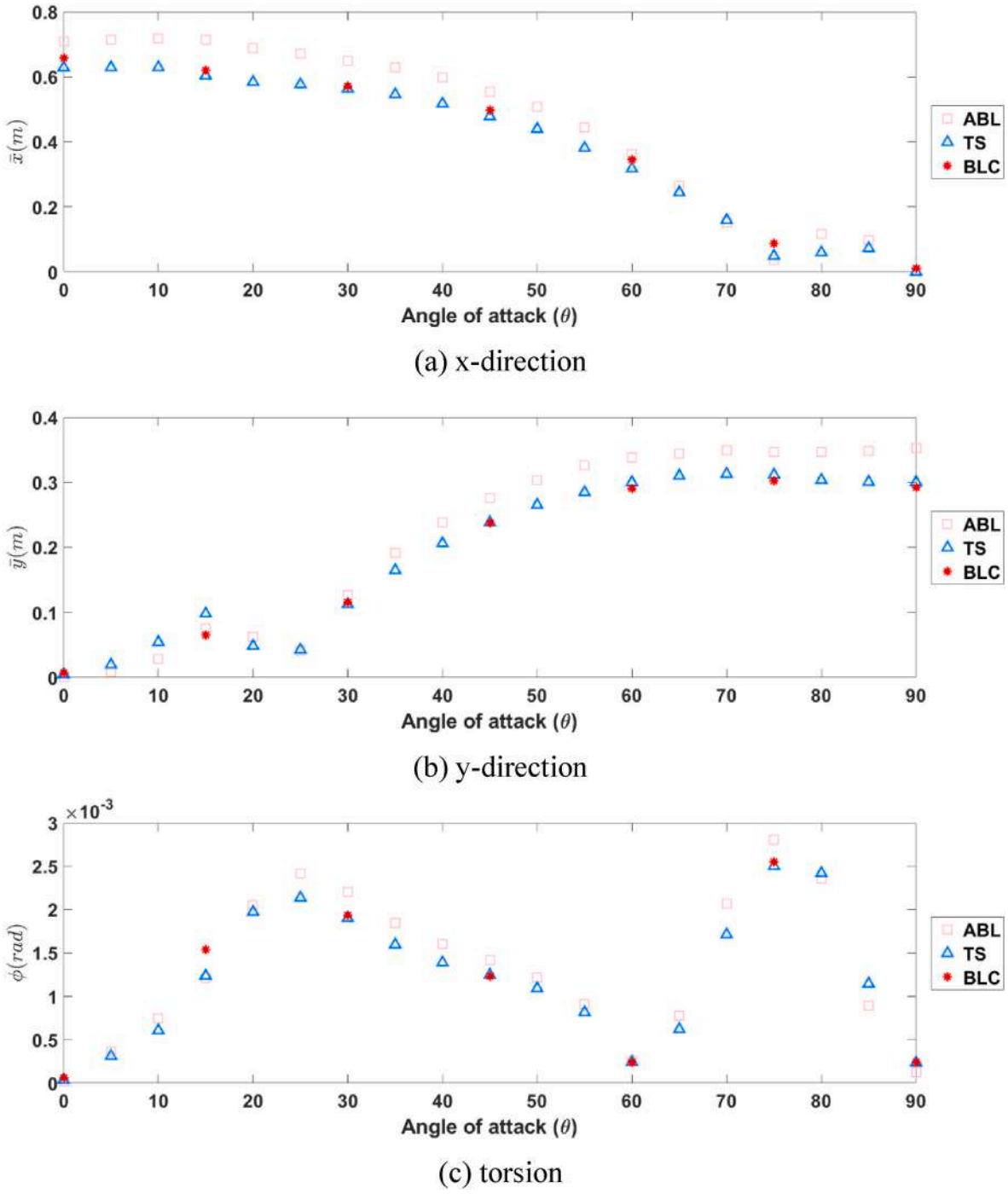

Fig. 19. Mean responses in the (a) x-direction, (b) y-direction and (c) torsion.

the wake frequency on the leeward face results in a larger squared spectrum value for the resonant component response. In the *y* direction, the differences in the squared spectrum values between the TS and ABL flows are less than in the *x* direction except for the angle of attack = 0°–10°. The squared spectrum value decreases with the reduced velocity in the ABL flow at all angle ranges. Most cases in the TS flow have the same tendency. Although insignificant, the angle of attack = 20°, 35°, and 70° shows that the largest resonant component response occurs when the reduced velocity is 7 instead of 8. The torsional response over the range 25°–60° in the TS flow are found to be larger than the ABL flow, and the differences caused by the reduced velocities are smaller, especially when the reduced velocity is larger than 5. When the angle of attack = 10° and 15°, the reduced velocity of 6 in the ABL flow produces the largest squared spectrum value, addressing again the effects caused by the lower turbulence intensity in the approaching winds. Resonant responses in all directions are greater for BLC conditions than for ABL or TS wind conditions.

3.2.4. *Peak responses*

The profile-shape effects caused by the nose-like flow have been examined component by component in the previous sections. It was found that only for a limited number of angle of attack the TS flow generated more significant responses in different components than the ABL flow. However, for directions where response is greatest the ABL flow leads to greater responses.

Fig. 22 shows the peak responses with respect to the angle of attack

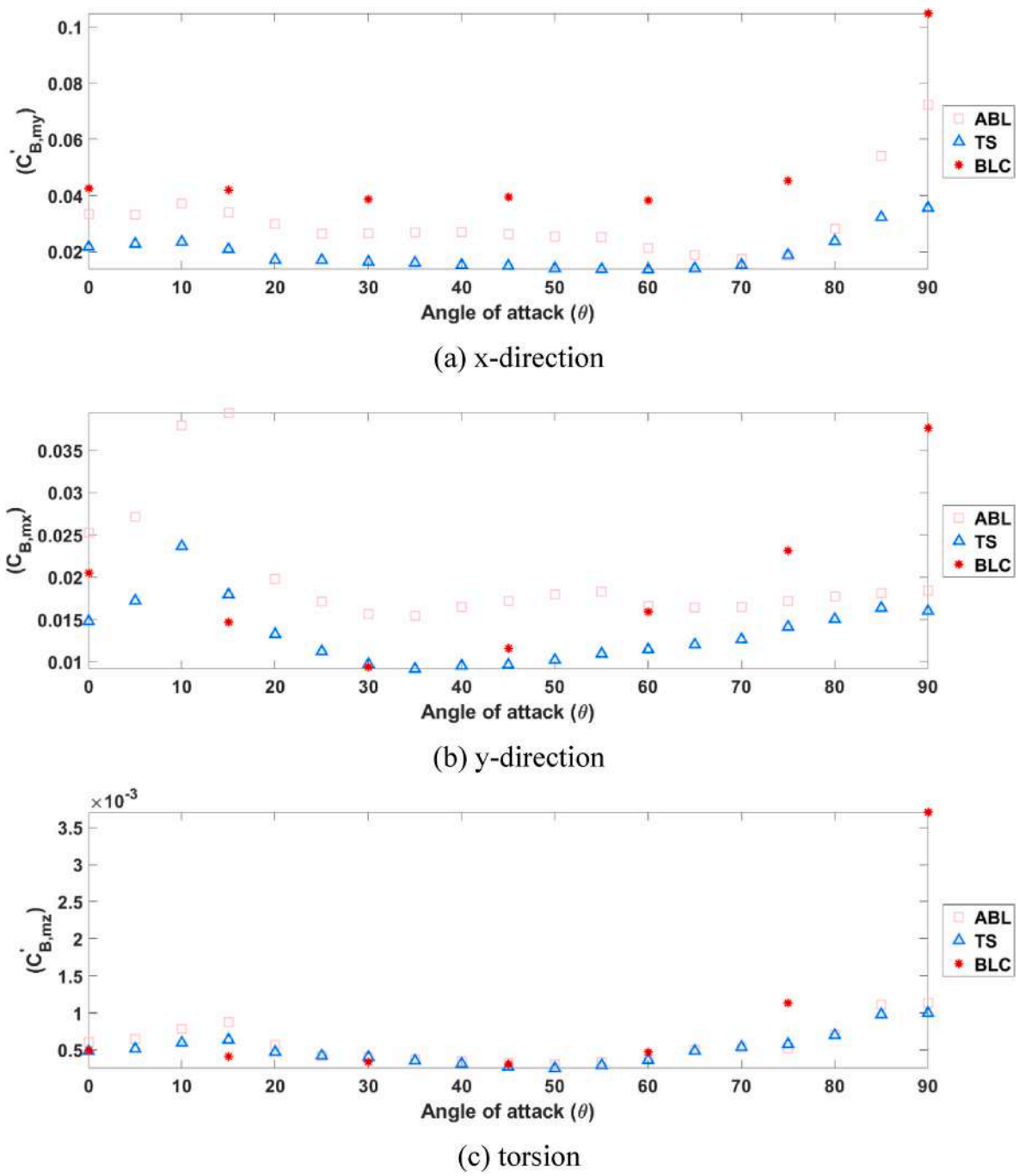

Fig. 20. Background component responses in the (a) x-direction, (b) y-direction and (c) torsion.

under various reduced velocities. The integrated responses in the three directions share the same tendency that the response magnitude increases as the reduced velocity increases. For the *x*-direction peak responses, the distributions of the TS flow are generally slightly lower than those of the ABL flow, except for the angle of attack = 70°–75° where they are marginally higher. For the *y*-direction peak responses, the distributions of the TS flow exhibit lower values without exception for all angles of attack. However, when the angle of attack is around 0°–10°, the TS flow produces considerably lower responses than the ABL case. The reason for this reduction can be linked back to results shown in Fig. 15(c), where no peak is shown due to vortex shedding from the building and the overall spectrum values are extremely low. The peak torsional responses exhibit the same pattern as that in the *y* direction when the angle of attack = 0°–10°. The angle range between 30° and 65° is identified to have larger peak responses in the φ for the TS flow when compared with the ABL flow. Two ranges are confirmed for the *x*-direction and the φ-direction peak responses. The former is 70°–75° while the latter is 30°–65°. From the viewpoint of engineering practice, although these two ranges of the angle of attack produce larger responses due to the nose-like profile flow, the corresponding response magnitudes are still smaller than other angles. Peak responses for the BLC flow case were uniformly larger than both other cases through all angles of attack.

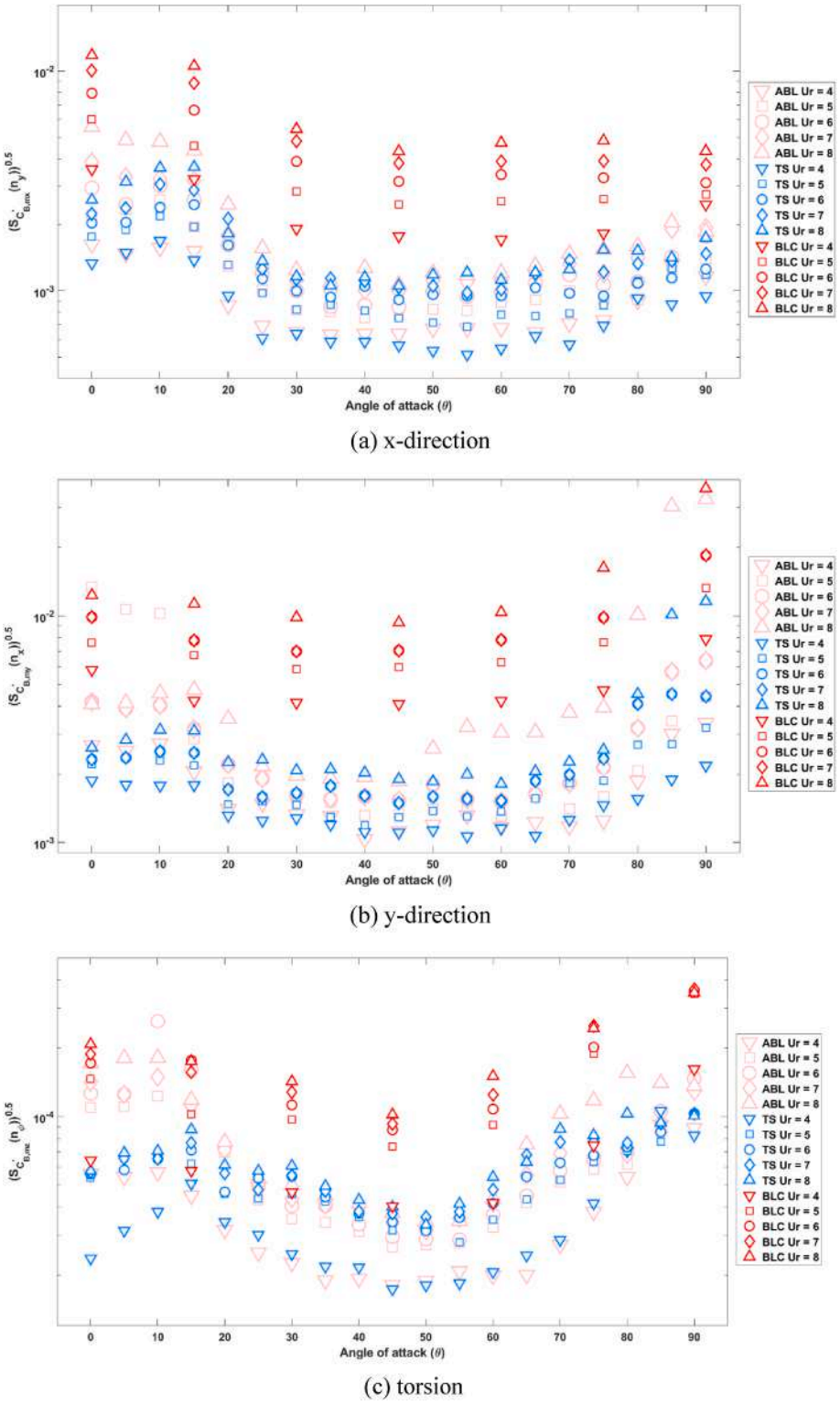

Fig. 21. Resonant response in the (a) x-direction, (b) y-direction and (c) torsional for various reduced velocities.

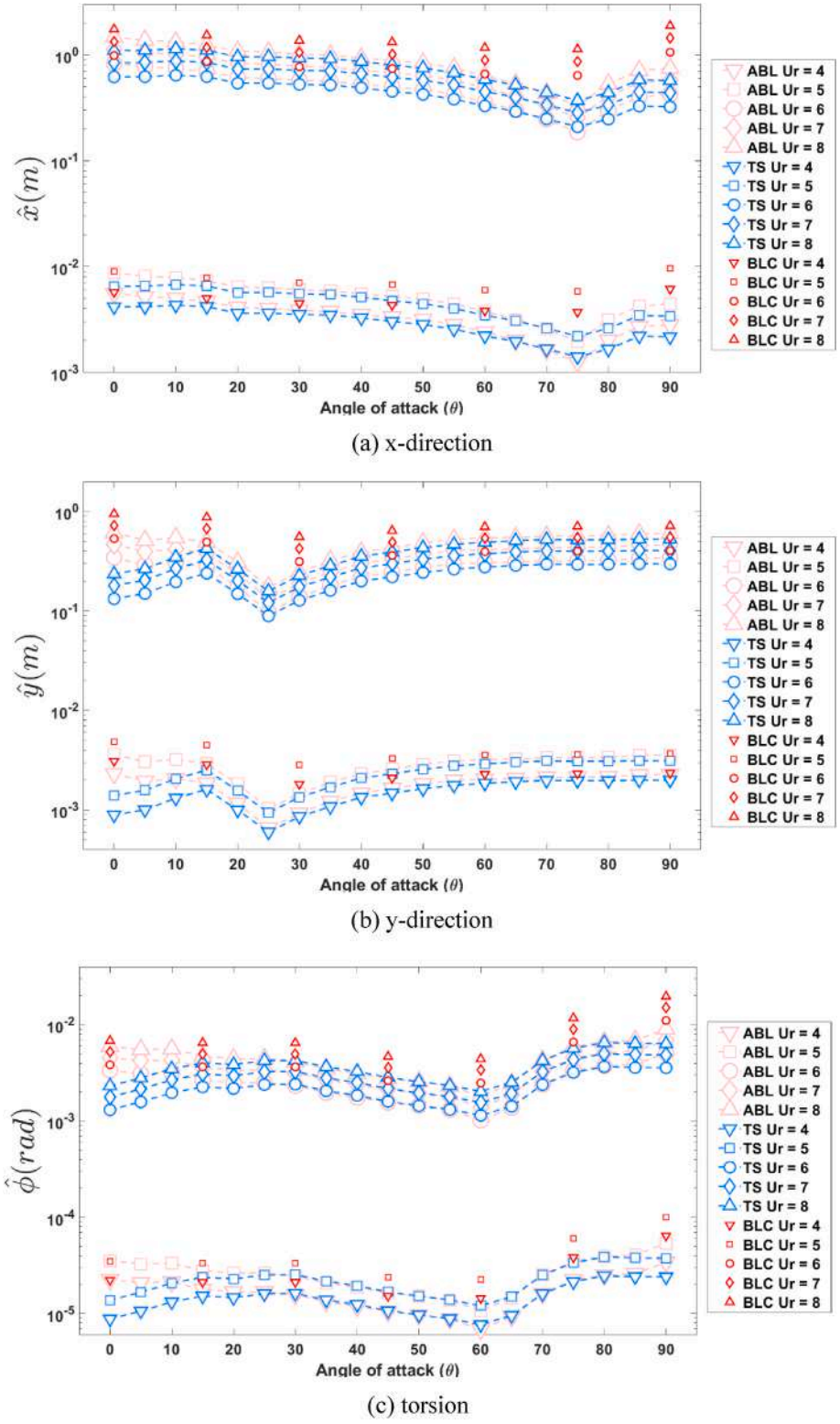

Fig. 22. Peak response in the (a) x-direction, (b) y-direction and (c) torsional for various reduced velocities.

4. Conclusions

This study examined the influence of incident velocity profile shape on the pressure distribution and estimated response of a generic tall building. This was done for the well-studied CAARC building subjected to three different flow fields, two with a mean velocity profile that resembles an 'open terrain' atmospheric boundary layer (BLC, ABL) and one that resembles a thunderstorm outflow-like wind field (TS). All tests were carried out in a multiple-fan wind tunnel at Tamkang University. The main findings of this research are:

1. The multiple-fan wind tunnel (MFWT) is a versatile tool for generating a range of desired wind fields. However, given the size of fans used in these tunnels, generation of the low frequency large scale gusts expected in an atmospheric boundary layer is challenging.
2. Notably different mean and fluctuating pressure coefficient distributions on the model building were observed for all three incident velocity fields with angles of flow incidence of 0° and 90°. Differences were noted between the two boundary layer profiles (BLC, ABL) on both the windward and wake region faces, with these attributed to inferred changes in the flow patterns around the building below the windward face stagnation zone and changes in the entrainment of flow into the wake due to differing levels of turbulence in the two fields. Differences in coefficients on the windward face between the simulated outflow-like wind field (TS) and the boundary layer fields could largely be explained by the differences in dynamic pressure in the incident velocity field. This observation supports findings from previous studies in boundary layer and uniform flow wind fields (Baines, 1963). Coefficient distributions on the other building faces were less easily linked to the incident velocity fields because of the differing wakes generated behind the body for each flow case and angle of incidence. Further research is required to characterize the dynamic flow structures in these wakes to better explain the observed loading patterns.
3. When estimating the wind-induced response (i.e., lateral displacements and torsional rotation) of the CAARC building to the three incident flow fields across a range of reduced velocities and wind incidence angles, the nose-like flow field (TS) led to lower responses in almost all cases. Differences between the response measured in the TS and ABL wind fields were most substantive for angles of attack between 0° and 15° where the width/depth dimension (and therefore wake width) of the building was greatest. Outside this angle range, peak TS responses were on average approximately 9% lower in the *x* direction, 10% lower in the *y* direction, and 3% lower in the rotational direction, than in the simulated ABL flow. Further, by dividing the estimated response into its mean, background and resonant components, it was found that much of the difference between flow fields was in the resonant component responses rather than the mean and background responses.

Much research remains to understand the loading of buildings during thunderstorm-generated wind events. Exploration of mean and dynamic load and response characteristics for a range of building geometries and for the range of transient velocity profiles potentially generated during outflow events – well beyond the single simplified steady flow case tested here - will be essential for adequately quantifying the kinematic load effects required for wind loading models such as that proposed by Kwon and Kareem (2009). While only a limited number of flow fields were examined here, it is believed that the important role of the wake structure in defining the resulting loading on the faces within this region, highlighted in this research, is an important step for guiding future research in this field. Additionally, the noted reduction in dynamic across-wind loading in the simulated outflow-like wind field when compared with generic boundary layer winds is an observation that warrants further exploration as to its generality.

Dedication

The authors desire to dedicate this paper to the memory of Professor Giovanni Solari, whose profound passion for science, strong dedication to his students, and genuine kindness will always be an example and an inspiration for those who were lucky enough to meet him.

CRediT authorship contribution statement

1. Yang Li: Experiment, Data curation, Formal analysis, Investigation, and Visualization.
2. Matthew S. Mason: Conceptualization, Investigation, and Writing (review and editing).
3. Hao-Yu Bin: Experiment, Data curation, and Visualization.
4. Yuan-Lung Lo: Conceptualization, Methodology, Data curation, Formal analysis, Investigation, Validation, Visualization, and Writing (original draft).

Declaration of competing interest

The authors declare that they have no known competing financial interests or personal relationships that could have appeared to influence the work reported in this paper.

Acknowledgments

This study is financially supported by the National Science and Technology Council research projects: MOST 107-2628-E-027-004-MY3 and MOST 110-2222-E-027-007-, and is technically supported by the Wind Engineering Research Center at Tamkang University.

References

Architectural Institute of Japan, 2015. Recommendations for Loads on Buildings. Architectural Institute of Japan, Tokyo, 2015.
Baines, W.D., 1963. Effects of velocity distributions on wind loads and flow patterns on buildings. In: Proceedings of International Conference on Wind Effects on Buildings and Structures (Teddington UK).
Butler, K., Cao, S., Kareem, A., Tamura, Y., Ozono, S., 2010. Surface pressure and wind load characteristics on prims immersed in a simulated transient gust front flow field. J. Wind Eng. Ind. Aerod. 98, 299–316.
Byers, H.R., Braham, R.R., 1949. The Thunderstorm: Final Report of the Thunderstorm Project. U.S. Government Printing Office, Washington, DC.
Canepa, F., Burlando, M., Solari, G., 2020. Vertical profile characteristics of thunderstorm outflows. J. Wind Eng. Ind. Aerod. 206, 102332.
Chay, M., Albermani, F., 2005. Dynamic response of a SDOF system subjected to simulated downburst winds. In: Proceedings of the 6th Asia-Pacific Conference on Wind Engineering, pp. 1562–1584. Seoul, Korea.
Chen, L., Letchford, C.W., 2004a. A deterministic-stochastic hybrid model of downbursts and its impact on a cantilevered structure. Eng. Struct. 26 (5), 619–629.
Chen, L., Letchford, C.W., 2004b. Parametric study on the alongwind response of the CAARC building to downbursts in the time domain. J. Wind Eng. Ind. Aerod. 92 (9), 703–724.
Choi, E.C.C., Hidayat, F.A., 2002. Dynamic response of structures to thunderstorm winds. Prog. Struct. Eng. Mater. 4, 408–416.
Choi, C.K., Kwon, D.K., 2003. Effects of corner cuts and angles of attack on the Strouhal number of rectangular cylinders. Wind Struct. 6 (2), 127–140.
Fujita, T.T., 1985. Downburst: Microburst and Macroburst. University of Chicago Press, Chicago, IL.
Fujita, T.T., 1990. Downburst: meteorological features and wind field characteristics. J. Wind Eng. Ind. Aerod. 36, 75–86.
Gunter, W.S., Schroeder, J.L., 2015. High-resolution full-scale measurements of thunderstorm outflow winds. J. Wind Eng. Ind. Aerod. 138, 13–26.
Hearst, R., Gomit, G., Ganapathisubramani, B., 2016. Effect of turbulence on the wake of a wall-mounted cube. J. Fluid Mech. 804, 513–530.
Hjelmfelt, M.R., 1988. Structure and life cycle of microburst outflows observed in Colorado. J. Appl. Meteorol. Climatol. 27 (8), 900–927.
Holmes, J.D., Forristall, G., McConochie, J., 2005. Dynamic response of structures to thunderstorm winds. In: Proceedings of the 10th Americas Conference on Wind Engineering. 10ACWE, Baton Rouge, La.
Holmes, J.D., Hangan, H.M., Schroeder, J.L., Letchford, C.W., Orwig, K.D., 2008. A forensic study of the Lubbock-Reese downdraft of 2002. Wind Struct. 11 (2), 137–152.
Huang, G., Chen, X., 2009. Wavelets-based estimation of multivariate evolutionary spectra and its application to nonstationary downburst winds. Eng. Struct. 31, 976–989.

Huang, G., Chen, X., Liao, H., Li, M., 2013. Predicting of tall building response to nonstationary winds using multiple wind speed samples. Wind Struct. 17 (2), 227–244.
Jesson, M., Sterling, M., Letchford, C., Haines, M., 2015a. Aerodynamic forces on generic buildings subject to transient, downburst-type winds. J. Wind Eng. Ind. Aerod. 137, 58–68.
Jesson, M., Sterling, M., Letchford, C., Baker, C., 2015b. Aerodynamic forces on the roofs of low-, mid- and high-rise buildings subject to transient winds. J. Wind Eng. Ind. Aerod. 143, 42–49.
Jubayer, C., Romanic, D., Hangan, H., 2019. Aerodynamic loading of a typical low-rise building for an experimental stationary and non-Gaussian impinging jet. Wind Struct. 28 (5), 315–329.
Kwon, D.K., Kareem, A., 2009. Gust-front factor: new framework for wind load effects on structures. J. Struct. Eng. ASCE 135 (6), 717–732.
Lambardo, F.T., Smith, D.A., Schroeder, J.L., Mehta, K.C., 2014. Thunderstorm characteristics of importance to wind engineering. J. Wind Eng. Ind. Aerod. 125, 121–132.
Letchford, C.W., Chay, M.T., 2002. Pressure distributions on a cube in a simulated thunderstorm downburst. Part B: moving downburst observations. J. Wind Eng. Ind. Aerod. 90 (7), 733–753.
Mason, M., James, D.L., Letchford, C.W., 2009. Wind pressure measurements on a cube subjected to pulsed impinging jet flow. Wind Struct. 12 (1), 77–88.
Ministry of Interior of Taiwan, 2015. Wind Resistant Designs on Buildings. Ministry of Interior of Taiwan, Taipei.
Nakamura, Y., Ohya, Y., 1984. The effects of turbulence on the mean flow past two-dimensional rectangular cylinders. J. Fluid Mech. 149, 255–273.
Sarpkaya, T., Kline, H., 1982. Impulsively-started flow about four types of bluff body. J. Fluid Eng. 104, 207–213.
Sarpkaya, T., Ihrig, C., 1986. Impulsively started steady flow about rectangular prisms: experiments and discrete vortex analysis. J. Fluid Eng. 108, 47–54.
Shirato, H., Maeda, K., Kato, Y., Takasugi, Y., 2009. Transient drag force on 2-d bluff bodies under gusty wind condition. In: The 7th Asia-Pacific Conference on Wind Engineering (Taipei, Taiwan).
Solari, G., Gaetano, P.D., Repetto, M.P., 2015. Thunderstorm response spectrum: fundamentals and case study. J. Wind Eng. Ind. Aerod. 143, 62–77.
Takeuchi, T., Maeda, J., 2013. Unsteady wind force on an elliptic cylinder subjected to a short-rise-time gust from steady flow. J. Wind Eng. Ind. Aerod. 122, 138–145.
Takeuchi, T., Maeda, J., Kawakami, R., Takeuchi, N., 2016. Effects of wind direction and roof shape on unsteady wind pressure on a low rise building under a short-rise-time gust. In: 8th International Colloquium on Bluff Body Aerodynamics and Applications. Northeastern University, Boston, Massachusetts, USA.
Tamura, Y., 2012. Amplitude dependency of damping in buildings and critical tip drift ratio. Int. J. High-Rise Build. 1 (1), 1–13.
Tamura, Y., Kareem, A., 2013. Advanced Structural Wind Engineering. Springer, Japan.
Tanaka, H., Lawen, N., 1986. Test on the CAARC standard tall building model with a length scale of 1 : 1000. J. Wind Eng. Ind. Aerod. 25 (1), 15–29.
Wardlaw, R.L., Moss, G.F., 1970. A Standard Tall Building Model for the Comparison of Simulated Natural Winds in Wind Tunnels, vol. 25. Commonwealth Advisory Aeronautical Research Council Report CC-662, Tech.
Wood, G.S., Kwok, K.C.S., Motteram, N.A., Fletcher, D.F., 2001. Physical and numerical modeling of thunderstorm downbursts. J. Wind Eng. Ind. Aerod. 89 (6), 535–552.
Yang, T., Mason, M.S., 2019. Aerodynamic characteristics of rectangular cylinders in steady and accelerating wind flow. J. Fluid Struct. 90, 246–262.